

Chapter 3 | Ti-Mo-Nb-Sn-Ta-Zr Thermodynamic Database

3.1 Introduction

The design of Ti-alloys for biomedical applications necessitates a completed thermodynamic database that will facilitate the prediction of phase compositions and fractions as a function of composition and temperature. However, there is no completed thermodynamic database for the Ti-Mo-Nb-Sn-Ta-Zr system and thus the present work aims at building a complete database with special focus on the Ti-rich alloys and bcc phase models. With this in mind the pure elements have been extensively studied and are widely adopted from the SGTE database [32]. The modeling of the binary systems has been widely documented with the exception of the Ta-Sn and Mo-Sn systems, while experimental phase boundary data is available for the ternary systems but little to no modeling has been completed. The Mo-Sn and Sn-Ta subsystems have high melting temperatures and little to no experimental data. In these cases, first-principles calculations based on DFT can be used to aid in modeling and supplement the lack of experimental data. The complete modeling of the Ta-Sn system is discussed in Chapter 4. In the present chapter, the thermodynamic descriptions of the Ti-Mo-Nb-Sn-Ta-Zr system are described.

While many of the alloys in this Ti system have been studied experimentally, yielding phase equilibrium data, only limited calorimetry data is available. With the present work focuses on bcc Ti-rich alloys, first-principles calculations based on DFT of the enthalpy of formation of the bcc phase were calculated. The thermodynamic

descriptions were built or evaluated using available experimental phase boundary data and present calculated thermochemical data. This work looks at evaluating new and previous models for the binary and Ti-containing ternary systems.

3.2 Computational details

First-principles results based on Density Functional Theory (DFT) are used to predict the enthalpy of formation of specific phases. In the present work, the enthalpy of formation of the bcc phase was calculated for the Ti-X and Ti-X-Y ($X \neq Y = Mo, Nb, Sn, Ta, Zr$) using the calculated energy of the pure elements in their SER states. For each binary system, 3 special quasirandom structures at different compositions, $Ti_{0.25}X_{0.75}$, $Ti_{0.50}X_{0.50}$, $Ti_{0.75}X_{0.25}$, were calculated where ($X = Mo, Nb, Sn, Ta, Zr$). The SQS were each 16-atom supercells that were previously generated and relaxed according to the methodology chapter [73]. For each binary system other dilute compositions were calculated, i.e. Ti-Mo 4 dilute structures ($Mo_{0.98}Ti_{0.02}$ 54-atoms, $Mo_{0.94}Ti_{0.06}$ 16-atoms, $Ti_{0.88}Mo_{0.12}$ 8-atoms, $Ti_{0.94}Mo_{0.06}$ 16-atoms), Ti-Nb 4 dilute structures ($Nb_{0.98}Ti_{0.02}$ 54-atoms, $Nb_{0.94}Ti_{0.06}$ 16-atoms, $Ti_{0.88}Nb_{0.12}$ 8-atoms, $Ti_{0.98}Nb_{0.02}$ 54-atoms), Ti-Sn 1 dilute structure ($Ti_{0.94}Sn_{0.06}$ 16-atoms), Ti-Ta 5 dilute structures ($Ta_{0.98}Ti_{0.02}$ 54-atoms, $Ta_{0.94}Ti_{0.06}$ 16-atoms, $Ti_{0.88}Ta_{0.12}$ 8-atoms, $Ti_{0.94}Ta_{0.06}$ 16-atoms, $Ti_{0.98}Ta_{0.02}$ 54-atoms), and Ti-Zr 2 dilute structures ($Zr_{0.94}Ti_{0.06}$ 16-atoms, $Ti_{0.98}Zr_{0.02}$ 54-atoms). For the Ti-X-Y ($X \neq Y = Mo, Nb, Sn, Ta, Zr$) ternary systems, three SQS calculations were completed at the compositions $Ti_{0.33}X_{0.33}Y_{0.33}$ (36-atom), $Ti_{0.50}X_{0.25}Y_{0.25}$ (32-atom), $Ti_{0.74}X_{0.13}Y_{0.13}$ (64-atom). The ternary SQS were previously generated and also relaxed according to the details outlined in the methodology chapter [74]. The DFT calculations are completed using VASP (Vienna ab-initio Simulation Package) [61]. The ion-electron interactions were described using the projector augmented wave (PAW) [62, 90] method. Based on the work of comparing X-C functionals (Figure 5.1) the exchange-correlation functional of the generalized gradient approach depicted by Perdew, Burke, and Ernzerhof (PBE) was employed [58]. For consistency, a 310 eV energy cutoff was adopted for all calculations, which is roughly 1.3 times higher than the default values suggested by VASP for the elements Ti, Mo, Nb, Sn, Ta, and Zr. The energy convergence criterion was 10^{-6} eV/atom, and the Monkhorst-Pack scheme is used for Brillouin zone sampling [61, 91]. The k-points grid for each calculation

are listed in appendix C.

3.3 Sn binaries and ternaries

The thermodynamic description of the Mo-Sn system has never been modeled and there is little to no experimental data available. With this fact, first-principles calculations can be used to fill in the missing data points. However, this is not a hugely important sub-system and the modeling will be part of the future work. The Ta-Sn system is modeled in chapter 4. For the Sn-Zr system, the thermodynamic description was previously modeled. However, these models do not use compatible sublattice modeling with the current database, for the hcp phase. While the, Sn-Nb and Ti-Sn binary systems have been previously modeled, Sn will only be included in small percentages to the overall Ti-based alloy so until the rest of Sn binaries are modeled Sn will not be included in the database.

3.4 Pure element calculation results

In order to build the Ti-Mo-Nb-Ta-Zr thermodynamic database, thermodynamic descriptions for all the binary systems are evaluated first for accuracy and model compatibility and incorporated into the database (see Chapter 2). In the present work, only thermodynamic descriptions for the Ti-containing ternary systems are generated, Ti-X-Y ($X \neq Y = Mo, Nb, Ta, Zr$). When applicable the previous thermodynamic descriptions of the non Ti-containing ternary systems are incorporated into the database. The only case of a thermodynamic description of a non Ti-containing ternary, from this system, available in literature is the Mo-Nb-Ta system [11], and it is incorporated here.

Table 3.1 shows the equilibrium properties, volume V_0 , energy E_0 , bulk modulus B , and the derivative of bulk modulus B' obtained from Eq. 2.6 at 0 °K. The energy E_0 and bulk modulus B are compared with previous first-principles calculations at 0 °K. The energy values between the present calculations and previous calculations vary by 0 to 0.1 eV/atom. The B results from the present calculations and previous calculations vary by at most 3 GPa. The variances between the E_0 and B are small and due to the fact that the previous calculations used slightly different input parameters such as a different exchange correlation functional (PBE vs PW91) and

higher energy cutoff values. Overall, the results are comparable. The B results from the present calculations at 0 °K are then compared with experimental values from literature. The variance between the B from the calculations and the B from experiments is also 3 GPa or less. This variance is attributed to the difference in temperature between the calculations and experiments. Based on the small variances shown in Table 3.1, the present calculations are deemed accurate.

3.5 Enthalpy of formation of bcc phase from first-principles

The enthalpies of formation of the bcc phase ($\text{bcc-}H_{Form}$) for the binary and ternary systems are presented in Table 3.2 and Table 3.3, respectively. As discussed in the methodology chapter, the $\text{bcc-}H_{Form}$ is calculated by Eq. 2.7. It is seen that Table 3.2 shows the first-principles results for $\text{bcc-}H_{Form}$ for the Ti-Mo system go from positive to negative to positive indicating the formation of a bcc miscibility gap. The first-principles results of the $\text{bcc-}H_{Form}$, for the Ti-Nb, Ti-Ta, and Ti-Zr systems, are positive across the entire composition range. Table 3.3 shows the values of the first-principles calculated $\text{bcc-}H_{Form}$. It is seen that the $\text{bcc-}H_{Form}$ values, for the Ti-Mo-Nb, Ti-Mo-Ta and Ti-Nb-Ta systems, go from positive at 100 at. % Ti to negative at 0 at. % Ti at the $X_{0.50}Y_{0.50}$ composition. The $\text{bcc-}H_{Form}$ values remain positive from 100 at. % Ti to 0 at. % Ti at the $X_{0.50}Y_{0.50}$ composition for the Ti-Mo-Zr, Ti-Nb-Zr, and Ti-Ta-Zr systems. For each system that the $\text{bcc-}H_{Form}$ is calculated, the values are compared with the CALPHAD modeling predictions and in some cases, are compared with experimentally obtained results. For some of the systems, when comparing the first-principles results of the $\text{bcc-}H_{Form}$ and the CALPAHD modeling prediction of the $\text{bcc-}H_{Form}$, no large discrepancies are seen and thus no new modeling is completed. In other cases, comparing the first-principles results of the $\text{bcc-}H_{Form}$ and the CALPAHD modeling prediction of the $\text{bcc-}H_{Form}$ showed larger discrepancies and then the first-principles $\text{bcc-}H_{Form}$ values are used to introduce new bcc interaction parameters. Each binary and Ti-containing ternary system is discussed in detail in the next sub sections below.

3.6 Thermodynamic modeling of the ten binary systems

3.6.1 Mo-Nb, Mo-Ta, Nb-Ta

Figure 3.1 shows the calculated phase diagrams for the Mo-Nb, Mo-Ta, and Nb-Ta systems from thermodynamic descriptions in the literature in comparison with experiments. The Mo-Nb, Mo-Ta and Nb-Ta descriptions are adopted from the modeling completed by Xiong et al. [11]. Xiong et al. [11] modeled these three binary systems and the ternary system, Mo-Nb-Ta. Binary interaction parameters were introduced for the liquid and bcc solution phases. The thermodynamic description, for the Mo-Nb system, was completed using differential thermal analysis experiments that measured both the liquidus and solidus temperatures [11]. Xiong et al. [11] decided to only use the experiments (shown in Figure 3.1 as X and +) that estimated the pure elements melting temperatures reasonably well when evaluating the binary interaction parameters. Xiong et al. [11] discussed, that after evaluating the binary interaction parameters for the Mo-Nb system, the experiments, shown by \circ , \triangle , \square , agreed well with the predicted phase diagram. Even though, the remaining experimental data points (\diamond , *) were quite low as compared to the predicted phase diagram, they were also quite low compared to all the other experiments [11] and were considered inaccurate. Thus Xiong et al. [11] concluded that the thermodynamic description generated is adequate at predicting the experimental data.

The thermodynamic description, for the Mo-Ta system, was completed using two sets of experimental data (\triangle , *, \diamond , \square) [11]. These particular experimental data points were chosen because they accurately measured the melting temperatures of Mo and Ta. The predicted phase diagram accurately reproduced the experimental data, with the exception of the experimental data [11] shown as " \circ ". This set of experimental data was 70 °K higher than all other experimental data. So as discussed by Xiong et. al. [11] the data were not thought to be accurate and were ignored.

For the Nb-Ta system, the thermodynamic description was completed using the experimental liquidus data [11] depicted in the figure by \circ , \triangle , and \square , because it predicts the melting temperatures of Nb and Ta accurately. The experimental

work which measured the solidus temperature (*) was not used because the melting temperatures of Nb and Ta showed discrepancy. The predicted phase diagram reproduces the experimental data well with the exception of the experimental work depicted by \diamond . This data was ignored because the values were 343 °K higher than the experimental values and thus it was determined by Xiong et al. [11] to be inaccurate. The present work agrees with the conclusion reached by Xiong et al. [11] and agrees that the phase diagrams reproduce the experimental data accurately. The sublattice models used by Xiong et al. [11] are compatible with the working database and the binary descriptions are incorporated without any changes. The interaction parameters for the binary systems incorporated into the database are listed in Table 3.4.

3.6.2 Mo-Zr, Nb-Zr and Ta-Zr

Figure 3.2 shows the predicted phase diagrams for the Mo-Zr, Nb-Zr, and Ta-Zr systems. For the Mo-Zr system, there are multiple previous thermodynamic descriptions and experimental results available. In the present work, the evaluation by Perez et al. [12] is chosen to be incorporated due to the fact that their model was also incorporated into the Ti-Mo-Zr ternary modeling found in the literature. The experimental data that is plotted determined the single-phase region, two-phase region, phase boundaries, and peritectic and eutectoid reactions. Perez et al. [12] went into more details on the available experimental data and discussing what was included in their evaluation. Perez et al. [12] introduced interaction parameters for the liquid, bcc, hcp, and Laves_C15 phases. The thermodynamic description generally reproduces all experimental data accurately.

The thermodynamic description, for the Nb-Zr system, was previously evaluated by Guillermet [13] in the literature. Figure 3.2 plots the predicted phase diagram with the solidus experimental data (\diamond , *) as well as the hcp solvus (Y, \circ) and bcc miscibility gap (\triangle , \square , +) data [13, 14, 21]. The description includes interaction parameters for the liquid, bcc, and hcp solution phases and accurately reproduces the experimental data.

For the Ta-Zr system, the thermodynamic description was also evaluated by Guillermet [15]. As discussed by Guillermet [15], there is quite a lot of experimental data, phase boundary results from at least five different papers and thermodynamic

results from three different papers [15]. Figure 3.2 plots the single-phase, two-phase, phase boundary, and solidus experimental data. Interaction parameters were introduced for the bcc, hcp, and liquid phases. The predicted phase diagram reproduces the data fairly well.

The thermodynamic descriptions of the three binary systems Mo-Zr, Nb-Zr, and Ta-Zr are determined to be accurate and the sublattice modeling used is compatible with the working database. Thus, the thermodynamic descriptions are incorporated into the database. The interaction parameters for the binary systems incorporated into the database are listed in Table 3.4.

3.6.3 Ti-Mo

The thermodynamic description in the COST 507 database, modeled by Saunders, [16] is looked at for the Ti-Mo system. This model is chosen because it is the model incorporated into the Ti-Mo-Zr thermodynamic modeling [24]. Interaction parameters were evaluated for the liquid, fcc, hcp, bcc (ordered bcc#1 and disordered bcc#2), AlM_D019, AlM-D022, and the AlTi-L10 phases. Figure 3.3a plots the predicted phase diagram [16] with the available experimental phase boundary data [17]. The phase boundary data is reproduced accurately. Figure 3.3b plots the predicted enthalpy of formation of the bcc phase (solid line) versus the results from the present first-principles calculations (circles) and are compared to the enthalpies of formation of the bcc phase obtained experimentally (red squares) [18]. The experimental bcc- H_{Form} values and the prediction from the model are at 300 °K while the first-principles results are at 0 °K. The experimental values of bcc- H_{Form} compare well with the calculations but get more negative closer to the Mo-rich side which can be attributed to the temperature difference. The enthalpy of formation of the bcc phase predicted varies from the first-principles calculations drastically between 20 and 80 at.% Mo. This discrepancy is due to the disagreement on the existence of a bcc miscibility gap. Previous experimental research, including the values plotted here, have shown an equilibrium bcc miscibility gap which would fit what is seen in the first-principles calculations [18, 92, 93]. While there is an interaction parameter for the bcc order and disorder, Saunders [16] did not model the bcc miscibility gap as being an equilibrium phase. While there are previous thermodynamic descriptions that model the bcc miscibility gap, Kar et al. [24]

showed that the experimental data from higher-component systems fit better with the description containing no miscibility gap. Based on this and the fact that the sublattice modeling is compatible with the working database, the thermodynamic description by Saunders [16] is adopted with no changes. The interaction parameters for the binary system incorporated into the database are listed in Table 3.4.

3.6.4 Ti-Nb

For the Ti-Nb system, its thermodynamic description is taken from Zhang et al. [19]. Originally the thermodynamic description by Kumar et al. [20, 21] was evaluated because it was used in the modeling of the Ti-Nb-Zr system. However, new experimental phase boundary data on the Nb rich side (Δ) showed the need to switch to the Zhang et al. [19] thermodynamic description. Zhang et al. [19] introduced interaction parameters for the Liquid, bcc, hcp and omega phases. Figure 3.4a plots the predicted phase diagram from Zhang et al. [19] versus solidus data (\square), hcp and bcc solvus data (\circ) [20, 21] and the new Nb-rich bcc solvus data (Δ) [19]. Figure 3.4b plots the predicted enthalpy of formation (solid line) versus the present first-principles calculations (circles) and are compared to the enthalpies of formation of the bcc phase obtained experimentally (red squares) [18]. The experimental bcc- H_{Form} values and the prediction from the model are at 300 °K while the first-principles results are at 0 °K. The experimental bcc- H_{Form} values compare well with the calculations and any variance can be attributed to the temperature difference. There is an average variance of 0.17 kJ/mol-atom between the DFT and CALPHAD predictions of th bcc- H_{Form} which is also attributed to the temperature difference. However, even with the variance, the CALPHAD prediction compares well with the DFT results and the phase diagram reproduces the experimental data accurately. The sublattice models are compatible and the thermodynamic description from Zhang et al. [19] is incorporated into the present database with no alterations. The interaction parameters for the binary system incorporated into the database are listed in Table 3.4.

3.6.5 Ti-Ta

The thermodynamic description, for the Ti-Ta system, is taken from the COST 507 database [16]. The predicted phase diagram is plotted in Figure 3.5a, with

the experimental liquidus and solidus data (\diamond and Y) as well as bcc and hcp solvus data (\triangle , \square , and \circ) for comparison. The evaluation includes interaction parameters for the fcc, hcp, liquid, AlM-D019, AlM-D022, AlTi-L10, and the bcc (ordered bcc#1, disordered bcc#2) phases [22]. The thermodynamic description reproduces the experimental data accurately. The enthalpy of formation of the bcc phase predicted by the CALPHAD modeling (solid line) is plotted with the first-principles results (circles) in Figure 3.5b. The CALPHAD prediction of the bcc- H_{Form} reproduces the results from first-principles reasonably well on the Ti-rich and Ta-rich sides. The first-principles results vary on an average by 0.17 kJ/mol-atom. However, the CALPHAD prediction is at 300 °K and the first-principles are at 0 °K which explains the variance. Based on these conclusions the thermodynamic description is deemed accurate and since the sublattice modeling is compatible, the thermodynamic description is incorporated into the database and not altered. The interaction parameters for the binary system incorporated into the database are listed in Table 3.4.

3.6.6 Ti-Zr

The thermodynamic description, of the Ti-Zr system, evaluated by Kumar et al. [21] is used in the present work. The model by Kumar et al. is chosen because it was used in the ternary modeling of the Ti-Mo-Zr and Ti-Nb-Zr systems. The evaluation introduces interaction parameters for the liquid, bcc, and hcp solution phases. Figure 3.6a plots the predicted phase diagram compared with phase boundary data for the bcc to hcp (\circ) phase transformation and solidus (\triangle). The thermodynamic description accurately reproduces the phase boundary data. When doing the evaluation, heat of transformation data was also used and was discussed by Kumar et al. [21]. Figure 3.6b plots the present first-principles results (circles) versus the CALPHAD prediction (solid line) for the bcc- H_{Form} . The first-principles results and CALPHAD modeling vary on average by 1.2 kJ/mol-atom. The variance is larger than the other binary alloys due to the instability of the bcc phase at both 0 °K and 300 °K for the Ti-Zr alloy but the calculations and CALPHAD prediction follow the same trend. Based on the agreement between the experimental data, no alterations were made to the thermodynamic description and with the sublattice modeling compatibility, it was incorporated into the database. The interaction

parameters for the binary system incorporated into the database are listed in Table 3.4.

3.7 Thermodynamic modeling of six Ti-containing ternary systems

3.7.1 Ti-Mo-Nb

A thermodynamic description, for the Ti-Mo-Nb system, has never been evaluated in the literature. Two experimental investigations were done on the Ti-Mo-Nb system at 873 °K and 1373 °K [25, 94]. While both investigations agree that the isothermal section at 1373 °K is solely the bcc phase, the investigations differed on the phase boundary at 873 °K. It is suspected that at such a low temperature the samples did not reach equilibrium which accounts for the discrepancy. Based on this, the binary interpolation of the isothermal sections at 1373 °K and 873 °K are plotted. The predicted phase diagram at 1373 °K agreed with the experimentally determined phase diagram to be solely the bcc phase. The phase diagram at 873 °K is plotted in Figure 3.7a. The discrepancy, at 873 °K, is the existence of the bcc miscibility gaps as well as what compositions the phase boundary lines lie at. The enthalpy of formation of the bcc phase is predicted using an interpolation of the binary interaction parameters (solid line) and plotted with the first-principles results, in Figure 3.7b, starting from a 50-50 mixture of the alloying elements ($\text{Mo}_{0.50}\text{Nb}_{0.50}$) to 100 at.% Ti. While the first-principles calculations are at 0 °K and the binary interpolation is at 300 °K, the calculation results are reproduced with the CALPHAD prediction. The prediction varies by less than 1.5 kJ/mol-atom for all the calculations except at $\text{Mo}_{0.50}\text{Nb}_{0.50}$. While the calculation varies substantially from the prediction at $\text{Mo}_{0.50}\text{Nb}_{0.50}$, in order to improve this, the Mo-Nb binary system would have to be adjusted. In the present work, no thermochemical data was used to ensure the accuracy of the non Ti-containing binary systems but the previous binary models were able to reproduce the phase boundary data as discussed above. Based on the discrepancy between the experimental data and the fact that the first-principles thermochemical calculations are reproduced well by the binary interpolation, no ternary interaction parameters are evaluated.

3.7.2 Ti-Mo-Ta

The thermodynamic description, of the Ti-Mo-Ta system, has not been previously modeled. The binary interpolation of the Ti-Mo-Ta alloy is plotted in Figure 3.8a at 873 °K. At 873 °K, the Ti-Mo-Ta alloy has the bcc and hcp solution phases with a tie triangle showing a three-phase region of bcc#1, bcc#2, and hcp. The experimental data agreed with the two-phase bcc-hcp region in the Ti-rich corner, but did not see a bcc miscibility gap or tie triangle [23]. Figure 3.8b shows the present first-principles calculations (circles) of the bcc- H_{Form} compared with the binary interpolation from the CALPHAD prediction (solid black line). The first-principles calculations line up fairly well with the CALPHAD prediction. However, due to the discrepancy of the experimental data ternary interaction parameters are investigated for the hcp and bcc phases using the first-principles results and experimental phase boundary data. The evaluated interaction parameters are listed in Table 3.4. After assessing the ternary interaction parameters, the isothermal section at 873 °K is again plotted and compared with experimental data in Figure 3.9a and zoomed in for Figure 3.9b. The enthalpy of formation of the newly assessed bcc phase is plotted as a red dashed line in Figure 3.8b. The assessment reproduces the first-principles results accurately. With the introduction of the interaction parameters the isothermal section fits with the experimental data [23]. The work by Nikitin [23] determined hcp phase boundary data plotted as \circ and two phase experimental data as \bullet . The two phase experimental data is reproduced by the present model. The hcp phase boundary data are not reproduced. However, reliable solid phase boundary data are difficult to obtain at such a low temperature and if the evaluation is altered to fit the data; it then over fits and stabilizes non-equilibrium phases.

3.7.3 Ti-Mo-Zr

The thermodynamic description of the Ti-Mo-Zr system was previously modeled by Kar et al. [24]. The same binary phases used in the modeling by Kar et al. are included in the present database. The phases in this ternary system are liquid, bcc, hcp, and Laves_C15. After interpolating the ternary system from the binary models and comparing to two sets of available experimental data, Kar et al. [24] introduced interaction parameters for the Laves_C15 phase. As discussed by Kar et al. [24],

there is phase boundary data at 1273 °K, from two papers [24]. The phase boundary data conflicts on how far out the two-phase region should extend toward the Ti-rich corner and whether there is a bcc miscibility gap. Due to the discrepancy, Kar et al. [24] decided not to introduce any bcc, liquid or hcp interaction parameters. The prediction of the phase diagram at 1273 °K by Kar et al. [24] is plotted in Figure 3.10a and compared with one set of phase boundary data [24]. The phase boundary data fits well on the Zr-Mo binary side but extends further in the Ti-rich corner. This is where the discrepancy lies, the other set of phase boundary data, not shown here, stops shorter than the prediction. The predicted enthalpy of formation of the bcc phase is plotted with the present first-principles results in Figure 3.10b. The first-principles results vary by 1.5 kJ/mol-atom from the CALPHAD prediction but the largest variance is seen at $\text{Mo}_{0.50}\text{Zr}_{0.50}$ which would only be improved by adjusting the binary Mo-Zr interaction parameters. Based on the available experimental data [24], the present first-principles calculations, and the conclusions from Kar et al. [24], the present work agrees with the introduction of the ternary Laves_C15 interaction parameters and lack of liquid, bcc and hcp ternary interaction parameters. The ternary Laves_C15 interaction parameters are listed in Table 3.4.

3.7.4 Ti-Nb-Ta

A thermodynamic description of the Ti-Nb-Ta system had not previously been evaluated in the literature but different isothermal sections had been estimated by Na et al. [26] using phase boundary data. The phase boundary data was obtained through x-ray diffraction. Na et al. [26] looked at samples at 823 °K and 673 °K. The authors [26] discussed that it is likely that the alloys at 673 °K never reach equilibrium conditions. The experimental results [26] were plotted on the binary interpolation in Figure 3.11a and Figure 3.11b. The bcc phase boundary data do not match with the binary interpolation. Figure 3.12 plots the enthalpy of formation of the bcc phase predicted by the binary interpolation (solid line) and the first-principles results (circles). The first-principles results vary from the binary interpolation. Due to the variance, ternary interaction parameters for the bcc and hcp phases are investigated. The evaluation was done using the 823 °K experimental data and the present first-principles calculations and the 673 °K data

was neglected. The evaluated ternary interaction parameters are listed in Table 3.4. After evaluation, the ternary isothermal sections are plotted with the phase boundary data in Figure 3.13a and Figure 3.13b. The isothermal sections at both 673 and 823 °K reproduce the experimental data [26] well. The assessed prediction (red dashed line in Figure 3.12) of the enthalpy of formation of the bcc phase also improves to accurately match the first-principles results.

3.7.5 Ti-Nb-Zr

The thermodynamic description, of the Ti-Nb-Zr system, was previously evaluated by multiple authors [21, 27]. In the present work, the binary interpolation of the ternary isothermal section at multiple temperatures are compared with experimental data [21, 27]. Figure 3.14a plots the isothermal section at 843 °K compared with the two-phase equilibria data and the tie-triangle phase boundary data [27]. The binary interpolation reproduced the data accurately. The enthalpy of formation of the bcc phase is plotted in Figure 3.14b. The CALPHAD prediction (solid line) of the bcc- H_{Form} varies on an average by 1.34 kJ/mol-atom from the first-principles results (circles). While there is some variance, it can be attributed to the temperature difference and overall the variance isn't large. So, the conclusion is reached to not introduce ternary interaction parameters.

3.7.6 Ti-Ta-Zr

For the Ti-Ta-Zr system, Lin et al. [28] calculated the isothermal sections using binary interpolations and introduced no interaction parameters. The isothermal sections at 1273 and 1773 °K are plotted in Figure 3.15a and Figure 3.15b, respectively. Experimental phase boundary data along the bcc miscibility gap at 1273 °K and single phase • and two phase region ● data using x-ray diffraction at 1773 ° are plotted to compare with the binary interpolations [28, 29]. The phase boundary data is reproduced accurately. Figure 3.16 plots the binary interpolation prediction (solid line) of the bcc- H_{Form} compared to the present first-principles calculations (circles). On average the first-principles varies by 3.69 kJ/mol-atom attributed partially to the temperature difference. While the variance is larger for the enthalpy of formation, the experimental data points [28] are reproduced and thus no ternary interaction parameters are evaluated

It is worth mentioning that all the interaction parameters for the Ti-Mo-Nb-Ta-Zr system are listed in Table 3.4 and combined into a single thermodynamic database (TDB) file in Appendix A.

3.8 Conclusion

The present work built a compatible thermodynamic database for the Ti-Mo-Nb-Sn-Ta-Zr system using descriptions of five pure elements (Ti, Mo, Nb, Ta, Zr), ten binary systems (Ti-Mo, Ti-Nb, Ti-Ta, Ti-Zr, Mo-Nb, Mo-Ta, Mo-Zr, Nb-Ta, Nb-Zr, Ta-Zr), and six Ti-containing ternary systems (Ti-Mo-Nb, Ti-Mo-Ta, Ti-Mo-Zr, Ti-Nb-Ta, Ti-Nb-Zr, Ti-Ta-Zr). Sn was excluded from the database due to the lack of modeling for the Sn binary systems. The Ta-Sn and Mo-Sn system lacked a thermodynamic description and the thermodynamic modeling of the Sn-Zr system is incompatible with the current database. The present work began modeling the Sn binaries with the Ta-Sn system discussed chapter 4. Until the binaries are properly modeled Sn was not included in the database which shouldn't affect the use of the database for biomedical applications since Sn will only be added to biomedical alloys in small percentages. The thermodynamic descriptions of the pure elements were adopted from the SGTE database [32]. All of the binary systems had previous thermodynamic descriptions available and the compatible descriptions were evaluated for accuracy and incorporated into the database. The binary interpolations of the Ti-containing ternary systems were plotted and compared with the available experimental data as well as the enthalpy of formation of the bcc phase calculated from first-principles based on DFT. The Ti-Sn-X systems (X = Mo, Nb, Ta, Zr) will be modeled in the future work once the Sn binaries are modeled. The binary interpolations of the Ti-Nb-Zr and Ti-Ta-Zr systems had previously been plotted but no interaction parameters had been introduced. The present evaluation agreed with the previous evaluations and no ternary interaction parameters were introduced. The Ti-Mo-Zr system had previously been modeled and the present work agreed with the evaluation. The Ti-Mo-Nb, Ti-Mo-Ta and Ti-Nb-Ta systems had never previously been modeled. The present work evaluated interaction parameters for the Ti-Mo-Ta and Ti-Nb-Ta systems but didn't introduce any interaction parameters for the Ti-Mo-Nb system. The thermodynamic descriptions were all incorporated into a complete database

that accurately predicts the phase stability of the Ti-Mo-Nb-Sn-Ta-Zr systems.

Table 3.1: Equilibrium properties volume V_0 , energy E_0 , bulk modulus B and the first derivative of bulk modulus with respect to pressure B' from the first-principles calculations for each pure elements in their SER state. The sv and pv refer to the electrons chosen as valance according to the VASP recommendations. The presently calculated results are also compared with available experimental data.

Phase	V_0 ($\text{\AA}^3/\text{atom}$)	E_0 (eV/atom)	B (GPa)	B'	Reference
hcp-Ti_sv	17.37	-7.80	113	3.54	This work
		-7.89	113		Calc 0 °K [95, 96]
			110		Expt 300 °K [97]
bcc-Mo_pv	15.91	-10.84	262	4.37	This work
		-10.86	262		Calc 0 °K [96, 98]
			261		Expt 300 °K [99]
bcc-Nb_sv	18.14	-10.22	171	3.78	This work
		-10.12	174		Calc 0 °K [96, 100]
			172		Expt 300 °K [99]
bcc-Ta_pv	18.32	-11.85	196	4.32	This work
		-11.85	194		Calc 0 °K [96, 101]
			196		Expt 300 °K [99]
hcp-Zr_sv	23.44	-8.51	94	3.13	This work
		-8.55	94		Calc 0 °K [96, 102–104]

Table 3.2: First-principles results at 0 °K for the enthalpy of formation (H_{Form}) of the bcc phase for different mole fractions (x) of alloying element X in the Ti-X binary systems (X = Mo, Nb, Ta, Zr).

Alloy	Type of Calc	H_{Form} (kJ/mol-atom)
Ti	Elemental	7.29
Mo, Nb, Ta	Elemental	0.00
Zr	Elemental	8.19
Ti _{0.94} Mo _{0.06}	Dilute	3.08
Ti _{0.88} Mo _{0.12}	Dilute	2.82
Ti _{0.75} Mo _{0.25}	SQS	1.12
Ti _{0.50} Mo _{0.50}	SQS	-3.67
Ti _{0.25} Mo _{0.75}	SQS	-5.18
Ti _{0.06} Mo _{0.94}	Dilute	1.79
Ti _{0.02} Mo _{0.98}	Dilute	5.82
Ti _{0.98} Nb _{0.02}	Dilute	6.92
Ti _{0.88} Nb _{0.12}	Dilute	5.88
Ti _{0.75} Nb _{0.25}	SQS	7.57
Ti _{0.50} Nb _{0.50}	SQS	8.54
Ti _{0.25} Nb _{0.75}	SQS	1.15
Ti _{0.06} Nb _{0.94}	Dilute	0.59
Ti _{0.02} Nb _{0.98}	Dilute	0.20
Ti _{0.98} Ta _{0.02}	Dilute	7.21
Ti _{0.94} Ta _{0.06}	Dilute	7.04
Ti _{0.88} Ta _{0.12}	Dilute	9.28
Ti _{0.75} Ta _{0.25}	SQS	4.89
Ti _{0.50} Ta _{0.50}	SQS	3.94
Ti _{0.25} Ta _{0.75}	SQS	3.10
Ti _{0.12} Ta _{0.88}	Dilute	0.94
Ti _{0.02} Ta _{0.98}	Dilute	0.28
Ti _{0.98} Zr _{0.02}	Dilute	5.49
Ti _{0.75} Zr _{0.25}	SQS	4.59
Ti _{0.50} Zr _{0.50}	SQS	1.94
Ti _{0.25} Zr _{0.75}	SQS	3.50
Ti _{0.06} Zr _{0.94}	Dilute	5.72

Table 3.3: First-principles results at 0 °K for the enthalpy of formation (H_{Form}) of the bcc phase for different mole fractions (x) of Ti in the Ti-X-Y ternary systems (X ≠ Y = Mo, Nb, Ta, Zr).

Alloy	Type of Calc	x(Ti)	H_{Form} (kJ/mol-atom)
Mo _{0.50} Nb _{0.50}	SQS	0.000	-38.69
Ti _{0.33} Mo _{0.33} Nb _{0.33}	SQS	0.333	5.08
Ti _{0.50} Mo _{0.25} Nb _{0.25}	SQS	0.500	-2.10
Ti _{0.74} Mo _{0.13} Nb _{0.13}	SQS	0.750	2.18
Mo _{0.50} Ta _{0.50}	SQS	0.000	-15.64
Ti _{0.33} Mo _{0.33} Ta _{0.33}	SQS	0.333	-5.34
Ti _{0.50} Mo _{0.25} Ta _{0.25}	SQS	0.500	-1.82
Ti _{0.74} Mo _{0.13} Ta _{0.13}	SQS	0.750	2.77
Mo _{0.50} Zr _{0.50}	SQS	0.000	10.31
Ti _{0.33} Mo _{0.33} Zr _{0.33}	SQS	0.333	8.36
Ti _{0.50} Mo _{0.25} Zr _{0.25}	SQS	0.500	7.73
Ti _{0.74} Mo _{0.13} Zr _{0.13}	SQS	0.750	6.82
Nb _{0.50} Ta _{0.50}	SQS	0.000	-0.41
Ti _{0.33} Nb _{0.33} Ta _{0.33}	SQS	0.333	1.82
Ti _{0.50} Nb _{0.25} Ta _{0.25}	SQS	0.500	3.80
Ti _{0.74} Nb _{0.13} Ta _{0.13}	SQS	0.750	5.59
Nb _{0.50} Zr _{0.50}	SQS	0.000	6.21
Ti _{0.33} Nb _{0.33} Zr _{0.33}	SQS	0.333	9.82
Ti _{0.50} Nb _{0.25} Zr _{0.25}	SQS	0.500	10.06
Ti _{0.74} Nb _{0.13} Zr _{0.13}	SQS	0.750	8.75
Ta _{0.50} Zr _{0.50}	SQS	0.000	5.75
Ti _{0.33} Ta _{0.33} Zr _{0.33}	SQS	0.333	2.98
Ti _{0.50} Ta _{0.25} Zr _{0.25}	SQS	0.500	2.79
Ti _{0.74} Ta _{0.13} Zr _{0.13}	SQS	0.750	0.79

Table 3.4: Modelled binary and ternary thermodynamic parameters for the Ti-Mo-Nb-Ta-Zr system. The thermodynamic description of pure elements is not included. The pure element functions, such as GFCCTI, describe the Gibbs energy (G) of the phase (FCC) for the element (TI) were adopted from the SGTE database [32] are listed in the Supplementary TDB (thermodynamic database) file.

Phase	Reference	Interaction Parameter
Liquid	[16]	$0_{Ti,Mo}^L = -9000.0 + 2.00 * T$
	[19]	$0_{Ti,Nb}^L = 7406.1$
	[16]	$0_{Ti,Ta}^L = 1000.0$
	[16]	$0_{Ti,Ta}^L = -7000.0$
	[21]	$0_{Ti,Zr}^L = -967.7$
	[11]	$0_{Mo,Nb}^L = 15253.7$
	[11]	$1_{Mo,Nb}^L = 10594.2$
	[11]	$0_{Mo,Ta}^L = 13978.9$
	[12]	$0_{Mo,Zr}^L = -24055.1 + 8.146 * T$
	[12]	$1_{Mo,Zr}^L = -5132.17 + 4.804 * T$
	[13]	$0_{Nb,Zr}^L = 10311.0$
	[13]	$1_{Nb,Zr}^L = 6709.0$
	[15]	$0_{Ta,Zr}^L = 13832.1$
	[15]	$1_{Ta,Zr}^L = -7150$
	[16]	$0_{Ti,Mo}^L = 2000.0$
	[16]	$1_{Ti,Mo}^L = -2000.0$
	[19]	$0_{Ti,Nb}^L = 13045.3$
	[16]	$0_{Ti,Ta}^L = 12000.0$
	[16]	$1_{Ti,Ta}^L = -2500.0$
	[21]	$0_{Ti,Zr}^L = -4346.2 + 5.49 * T$
	[11]	$0_{Mo,Nb}^L = -68202.6 + 29.86 * T$
	[11]	$1_{Mo,Nb}^L = 8201.3$
	[11]	$0_{Mo,Ta}^L = -75129.2 + 30.00 * T$
	[11]	$1_{Mo,Ta}^L = 6039.2$
	[12]	$0_{Mo,Zr}^L = 17936.0 + 3.10 * T$
	[12]	$1_{Mo,Zr}^L = -991.0 + 4.30 * T$
	[11]	$0_{Nb,Ta}^L = 1298.0$
	[13]	$0_{Nb,Zr}^L = 15911.0 + 3.35 * T$

Table 3.4: Modelled binary and ternary thermodynamic parameters for the Ti-Mo-Nb-Ta-Zr system. The thermodynamic description of pure elements is not included. The pure element functions, such as GFCCTI, describe the Gibbs energy (G) of the phase (FCC) for the element (TI) were adopted from the SGTE database [32] are listed in the Supplementary TDB (thermodynamic database) file.

Phase	Reference	Interaction Parameter
	[13]	$1_{Nb,Zr}^L = 3919.0 - 1.09 * T$
	[15]	$0_{Ta,Zr}^L = 29499.6 + 2.67 * T$
	[15]	$1_{Ta,Zr}^L = -4396.2 + 4.43 * T$
	[15]	$2_{Ta,Zr}^L = -6353.3 + 4.91 * T$
	This work	$0_{Ti,Mo,Ta}^L = -154731.2$
	This work	$0_{Nb,Ta,Ti}^L = -136603.3$
	This work	$1_{Nb,Ta,Ti}^L = -136602.7$
hcp	[16]	$0_{Ti,Mo}^L = 22760.0 - 6.00 * T$
	[19]	$0_{Ti,Nb}^L = 11742.4$
	[16]	$0_{Ti,Ta}^L = 8500.0$
	[21]	$0_{Ti,Zr}^L = 5133.0$
	[12]	$0_{Mo,Zr}^L = 26753.8 + 4.56 * T$
fcc	[13]	$0_{Nb,Zr}^L = 24411.0$
	[15]	$0_{Ta,Zr}^L = 30051.7$
	[16]	$0_{Ti,Mo}^L = 16500.0$
	[16]	$0_{Ti,Ta}^L = 8500.0$
	[16]	$0_{Ti:Ti}^L = 4 * GFCCTI$
Al3M_D022	[16]	$0_{Mo:Mo}^L = 4 * GFCCMO$
	[16]	$0_{Ti:Mo}^L = GFCCMO + 3.0 * GFCCTI$
	[16]	$0_{Mo:Ti}^L = 3.0 * GFCCMO + GFCCTI$
	[16]	$0_{Ti:Ta}^L = GFCCTA + 3.0 * GFCCTI$
	[16]	$0_{Ti:Ti}^L = 4.0 + 4.0 * GHserti$
AlM_D019	[16]	$0_{Mo:Mo}^L = 4.0 * GHCPMO$
	[16]	$0_{Ta:Ta}^L = 4.0 * GHCPTA$
	[16]	$0_{Ti:Mo}^L = 17072.0 - 4.5 * T + GHCPMO + 3.0 * GHserti$
	[16]	$0_{Mo:Ti}^L = 17072.0 - 4.5 * T + 3.0 * GHCPMO + GHserti$
	[16]	$0_{Ti:Ta}^L = 6376.0 + GHCPTA + 3.0 * GHserti$
	[16]	$0_{Ta:Ti}^L = 6376.0 + 3.0 * GHCPTA + GHserti$

Table 3.4: Modelled binary and ternary thermodynamic parameters for the Ti-Mo-Nb-Ta-Zr system. The thermodynamic description of pure elements is not included. The pure element functions, such as GFCCTI, describe the Gibbs energy (G) of the phase (FCC) for the element (TI) were adopted from the SGTE database [32] are listed in the Supplementary TDB (thermodynamic database) file.

Phase	Reference	Interaction Parameter
	[16]	$0_{Ti:Mo}^L = 51212.0 - 13.5 * T$
	[16]	$0_{Mo,Ti:Ti}^L = 51212.0 - 13.5 * T$
	[16]	$0_{Mo:Mo,Ti}^L = 5692.0 - 1.5 * T$
	[16]	$0_{Ti:Ti,Mo}^L = 5692.0 - 1.5 * T$
	[16]	$0_{Ta,Ti:Ta}^L = 19128.0$
	[16]	$0_{Ta,Ti:Ti}^L = 19128.0$
	[16]	$0_{Ta:Ta,Ti}^L = 2128.0$
	[16]	$0_{TI:Ta,Ti}^L = 2128.0$
AlTi	[16]	$0_{Ti:Ti}^L = 2.0 * GFCCTI$
	[16]	$0_{Mo:Mo}^L = 2.0 * GFCCMO$
	[16]	$0_{Ta:Ta}^L = 2.0 * GFCCTA$
	[16]	$0_{Ti:Mo}^L = 8250.0 + GFCCMO + GFCCTI$
	[16]	$0_{Mo:Ti}^L = 8250.0 + GFCCMO + GFCCTI$
	[16]	$0_{Ti:Ta}^L = 4250.0 + GFCCTA + GFCCTI$
	[16]	$0_{Ta:Ti}^L = 4250.0 + GFCCTA + GFCCTI$
	[16]	$0_{Mo,Ti:Mo}^L = 8250.0$
	[16]	$0_{Mo,Ti:Ti}^L = 8250.0$
	[16]	$0_{Mo:Mo,Ti}^L = 8250.0$
	[16]	$0_{Ti:Mo,Ti}^L = 8250.0$
	[16]	$0_{Ta,Ti:Ta}^L = 4250.0$
	[16]	$0_{Ta,Ti:Ti}^L = 4250.0$
	[16]	$0_{Ta:Ta,Ti}^L = 4250.0$
	[16]	$0_{Ti:Ta,Ti}^L = 4250.0$
bcc#2	[16]	$0_{Ti:Mo}^L = 10000.0$
disordered phase	[16]	$0_{Mo:Ti}^L = 10000.0$
	[16]	$0_{Ti:Ta}^L = 5000.0$
	[16]	$0_{Ta:Ti}^L = 5000.0$
Laves_C15	[24]	$0_{Ti:Ti}^L = 15000.0 + 3.0 * GHSERTI$

Table 3.4: Modelled binary and ternary thermodynamic parameters for the Ti-Mo-Nb-Ta-Zr system. The thermodynamic description of pure elements is not included. The pure element functions, such as GFCCTI, describe the Gibbs energy (G) of the phase (FCC) for the element (TI) were adopted from the SGTE database [32] are listed in the Supplementary TDB (thermodynamic database) file.

Phase	Reference	Interaction Parameter
	[12]	$0_{Mo:Mo}^L = 15000.0 + 3.0 * GHSERMO$
	[12]	$0_{Zr:Zr}^L = 15000.0 + 3.0 * GHSERZR$
	[24]	$0_{Ti:Mo}^L = 15000.0 + GHSERMO$ + $2.0 * GHserti$
	[24]	$0_{Mo:Ti}^L = 15000.0$ + $2.0 * GHSERMO + GHserti$
	[24]	$0_{Ti:Zr}^L = 9000.0$ + $GHSERZR + 2.0 * GHserti$
	[24]	$0_{Zr:Ti}^L = 15000.0 + 2.0 * GHSERZR + GHserti$
	[12]	$0_{Mo:Zr}^L = -21734.8 + 0.14 * T$ + $GHSERZR + 2.0 * GHSERMO$
	[12]	$0_{Zr:Mo}^L = 21734.8 - 0.14 * T$ + $2.0 * GHSERZR + GHSERMO$
	[12]	$0_{Mo:Mo,Zr}^L = 60000.0$
	[12]	$0_{Zr:Mo,Zr}^L = 60000.0$
	[12]	$0_{Mo,Zr:Mo}^L = 100000.0$
	[12]	$0_{Mo,Zr:Zr}^L = 100000.0$
	[24]	$0_{Ti:Mo,Zr}^L = 60000.0$
	[24]	$0_{Mo,Zr:Ti}^L = 100000.0$
omega	[19]	$0_{Ti}^L = 1886.7 - 0.15 * T + GHserti$
	[19]	$0_{Nb}^L = 15000.0 + 2.4 * T + GHSERNB$
	[32]	$0_{Zr}^L = -8878.082 + 144.432234 * T$ $- 26.8556 * T * LN(T) - .002799446 * T2 + 38376 * T - 1$ $298.15 < T < 2128$
		$- 29500.524 + 265.290858 * T - 42.144 * T * LN(T)$ $+ 7.17445E + 31 * T - 9$
		$2128 < T < 6000$
	[19]	$0LTi, Nb = -3775.9$

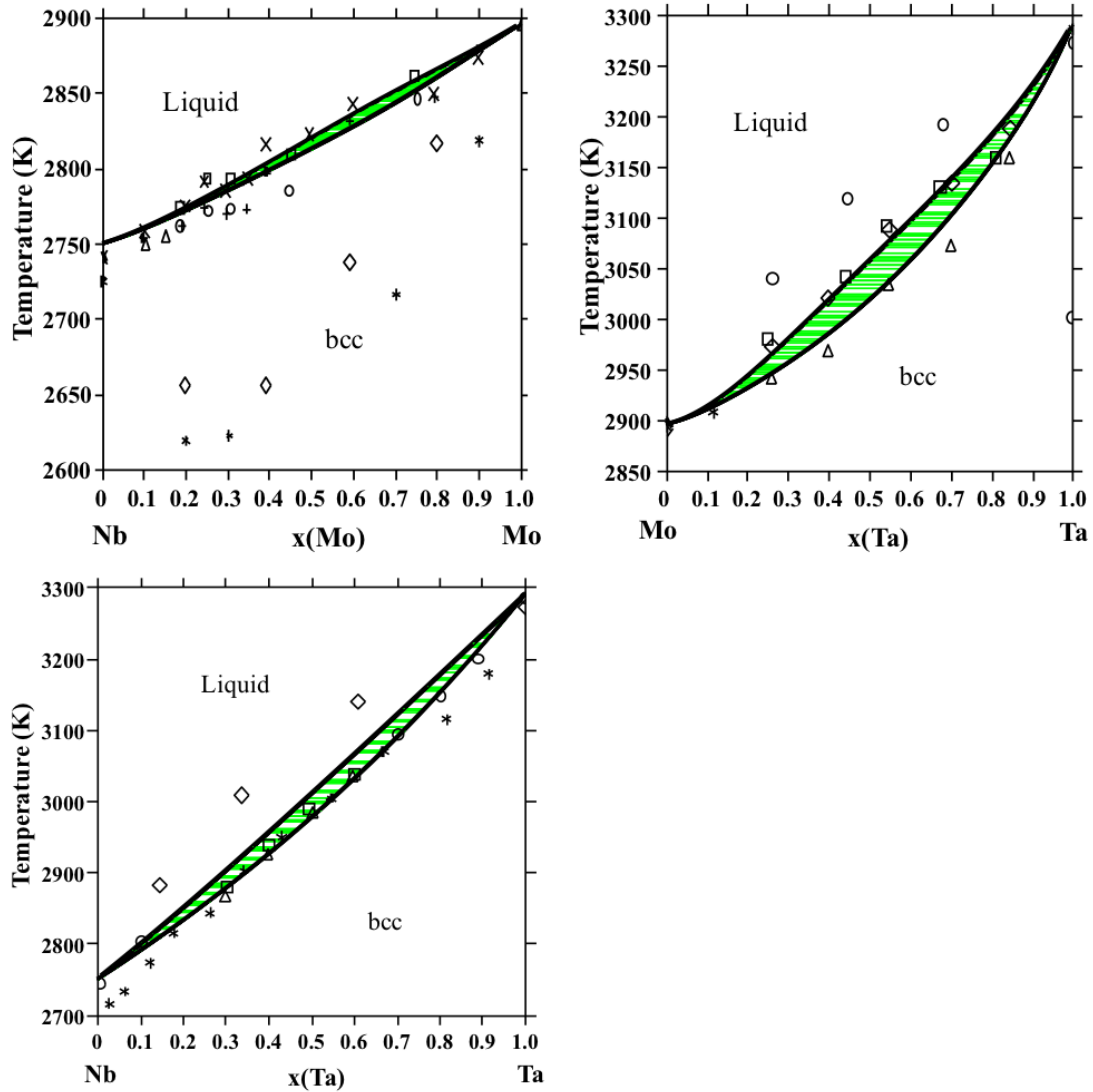


Figure 3.1: Previously modeled thermodynamic descriptions of the Mo-Nb (a) [11], Mo-Ta (b) [11] and Nb-Ta (c) [11] binary systems in comparison with available liquidus and solidus phase boundary experimental data to ensure accuracy (as detailed in [11]).

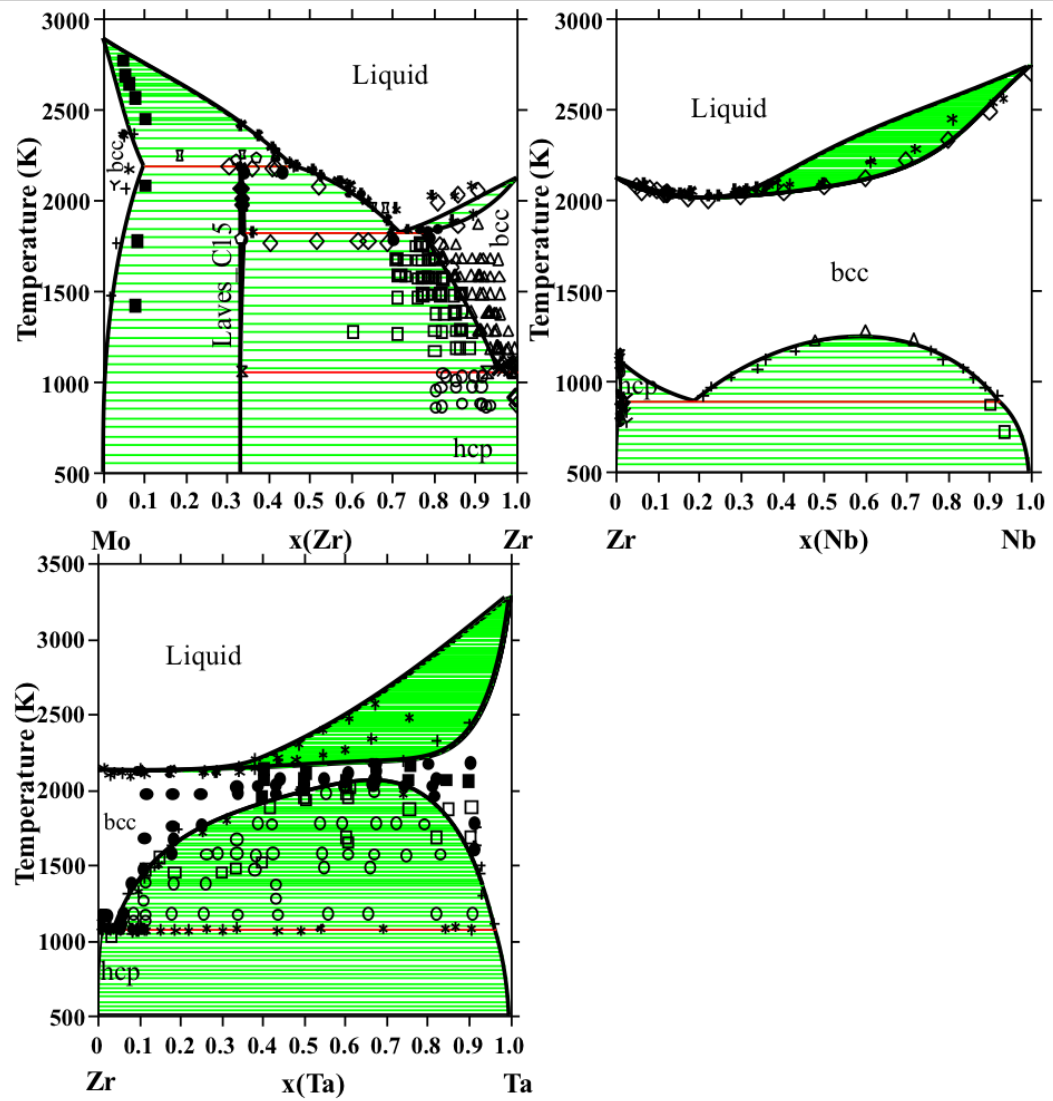


Figure 3.2: Previously modeled thermodynamic description of the Mo-Zr [12] system is plotted with phase boundary, reaction, single phase and two phase experimental data. The previously modeled Nb-Zr [13, 14] system is plotted with solidus, hcp solvus and bcc solvus experimental data. The previously modeled Ta-Zr [15] system is plotted with single-phase, two-phase, phase boundary and solidus experimental data (detailed in the mentioned references).

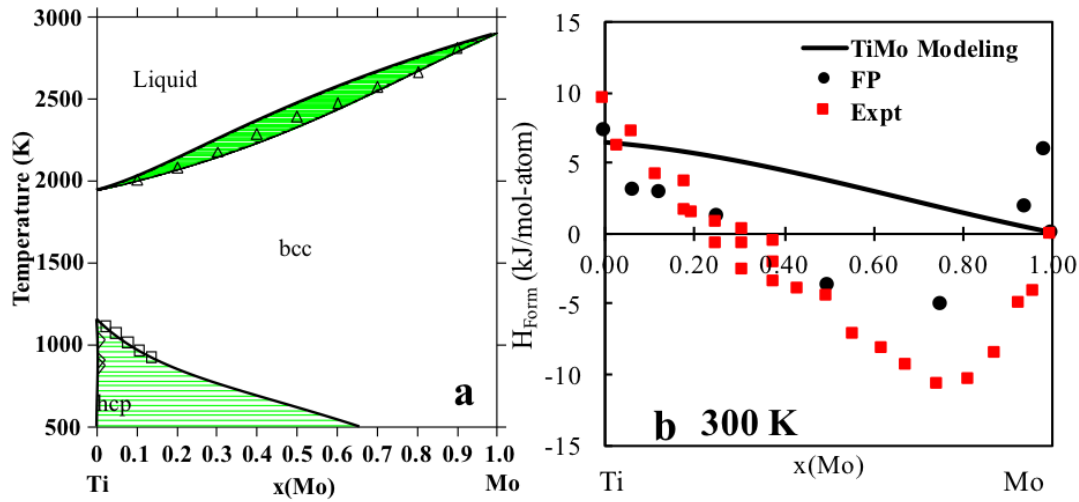


Figure 3.3: Previously modeled thermodynamic description of the Ti-Mo system versus available phase boundary and solidus experimental data to ensure accuracy [16, 17] (a), and enthalpy of formation of the bcc phase predicted by the previous thermodynamic modeling (solid line) at 300 °K versus the present first-principles calculations (circles) at 0 °K and compared with the enthalpy of formation of the bcc phase obtained from experiments [18] (b).

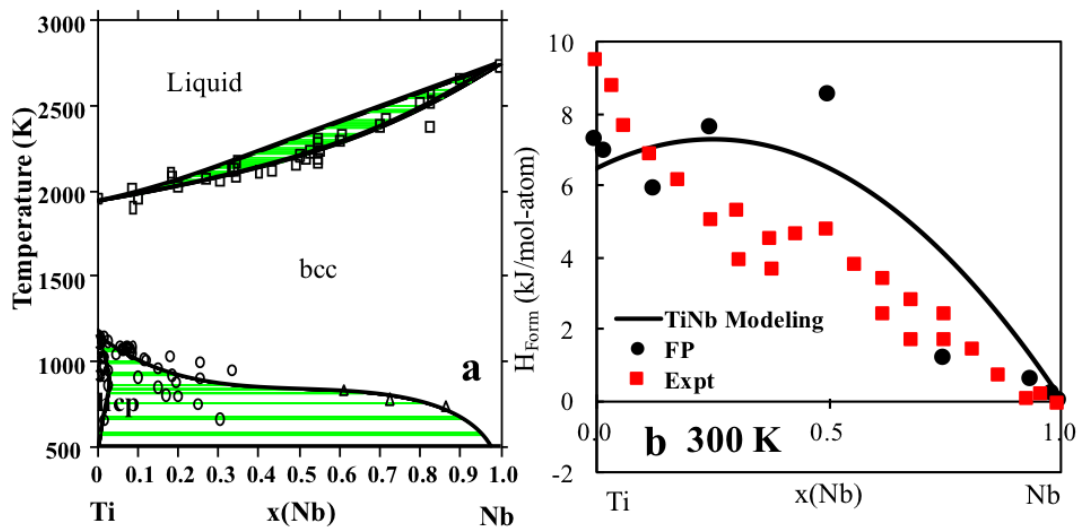


Figure 3.4: Previously modeled thermodynamic description of the Ti-Nb system versus available phase boundary and solidus experimental data to ensure accuracy [19–21][20,48] (a), and enthalpy of formation of the bcc phase predicted by the previous thermodynamic modeling (solid line) at 300 °K versus the present first-principles calculations (circles) at 0 °K compared with the enthalpy of formation of the bcc phase obtained from experiments [18] (b).

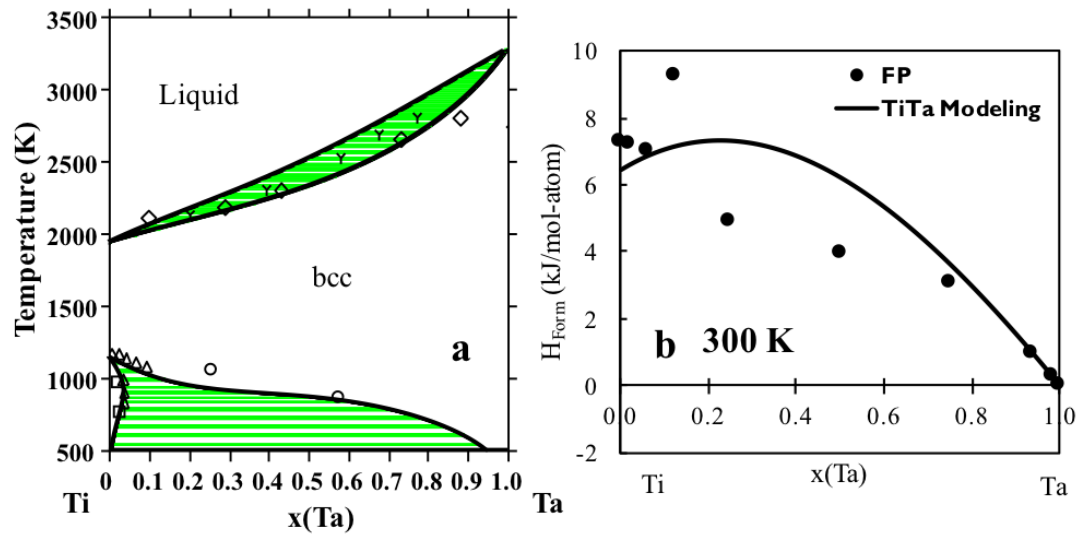


Figure 3.5: Previously modeled thermodynamic description of the Ti-Ta system versus available phase boundary and solidus experimental data to ensure accuracy [16, 22] (a), and enthalpy of formation of the bcc phase predicted by the previous thermodynamic modeling (solid line) at 300 °K versus the present first-principles calculations (circles) at 0 °K (b).

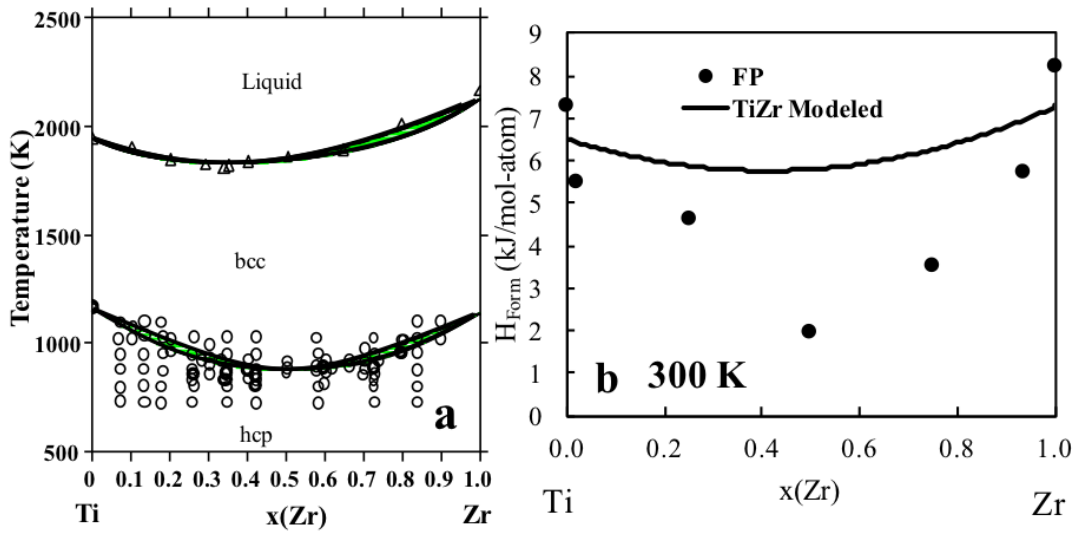


Figure 3.6: Previously modeled thermodynamic description of the Ti-Zr system versus available phase boundary and solidus experimental data to ensure accuracy [21] (a), and enthalpy of formation of the bcc phase predicted by the previous thermodynamic modeling (solid line) at 300 °K versus the present first-principles calculations (circles) at 0 °K (b).

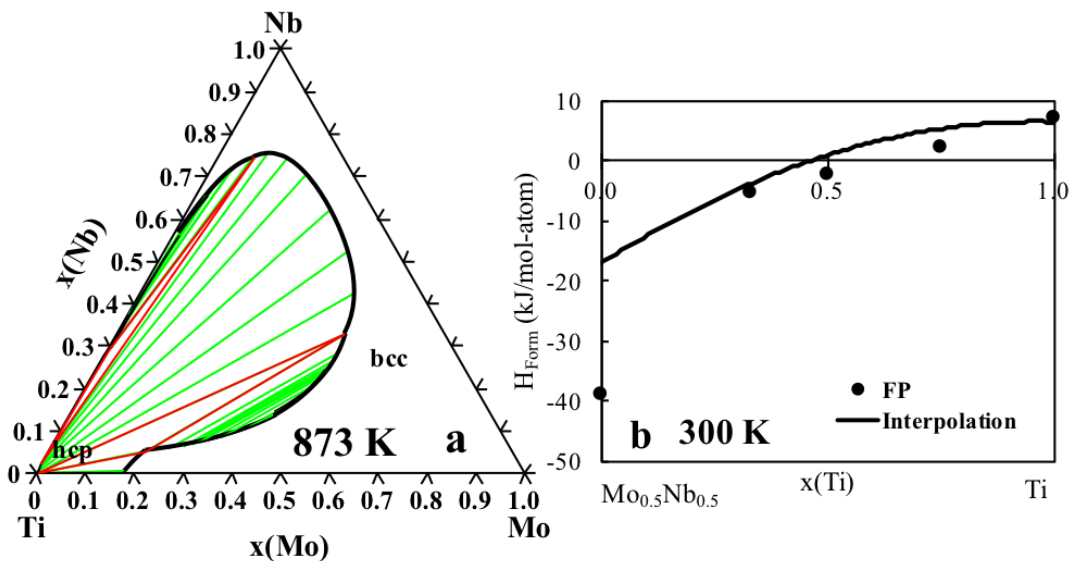


Figure 3.7: Binary interpolation of the isothermal section of the Ti-Mo-Nb system plotted at 873 °K (a), and enthalpy of formation of the bcc phase predicted by the binary interpolation of the thermodynamic modeling (solid line) at 300 °K versus the present first-principles calculations (circles) at 0 °K (b).

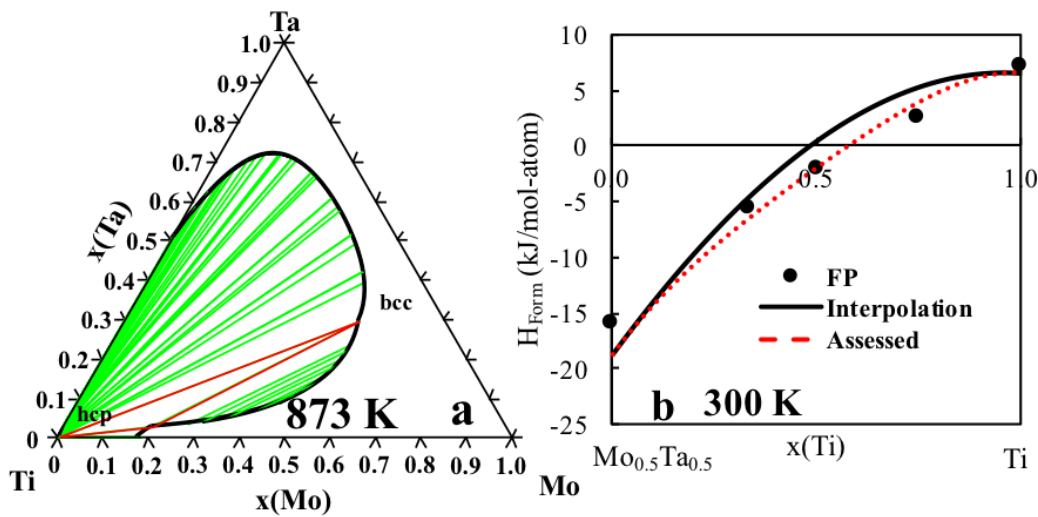


Figure 3.8: Binary interpolation of the isothermal section of the Ti-Mo-Ta system plotted at 873 °K (a), and enthalpy of formation of the bcc phase predicted by the previous thermodynamic modeling (solid line) at 300 °K and the ternary assessed thermodynamic modeling (red dotted line) versus the present first-principles calculations (circles) at 0 °K (b).

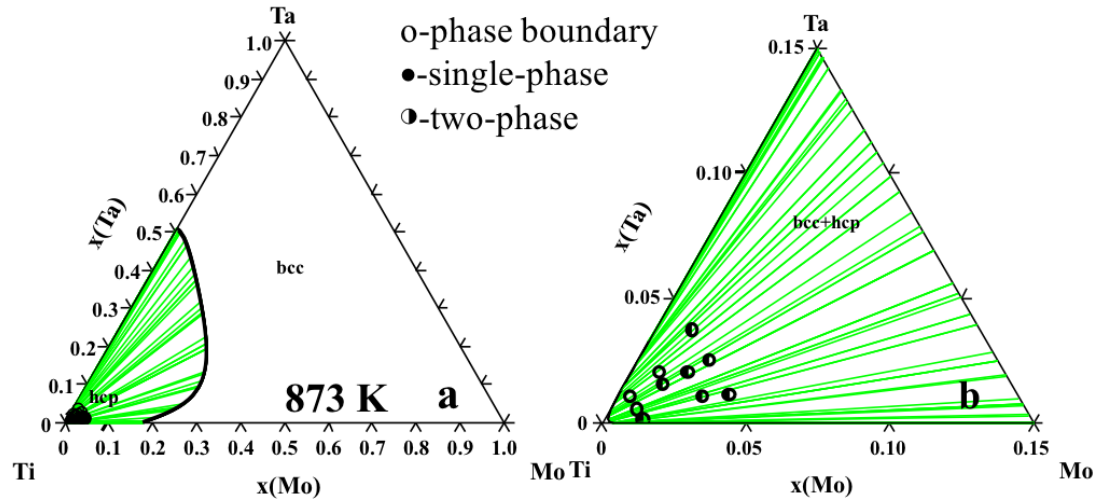


Figure 3.9: Ternary assessed isothermal section of the Ti-Mo-Ta system plotted at 873 °K (a), and zoomed in ternary assessed isothermal section at 873 °K (b) with the phase boundary and two-phase region experimental data [23] to ensure accuracy of the ternary assessment.

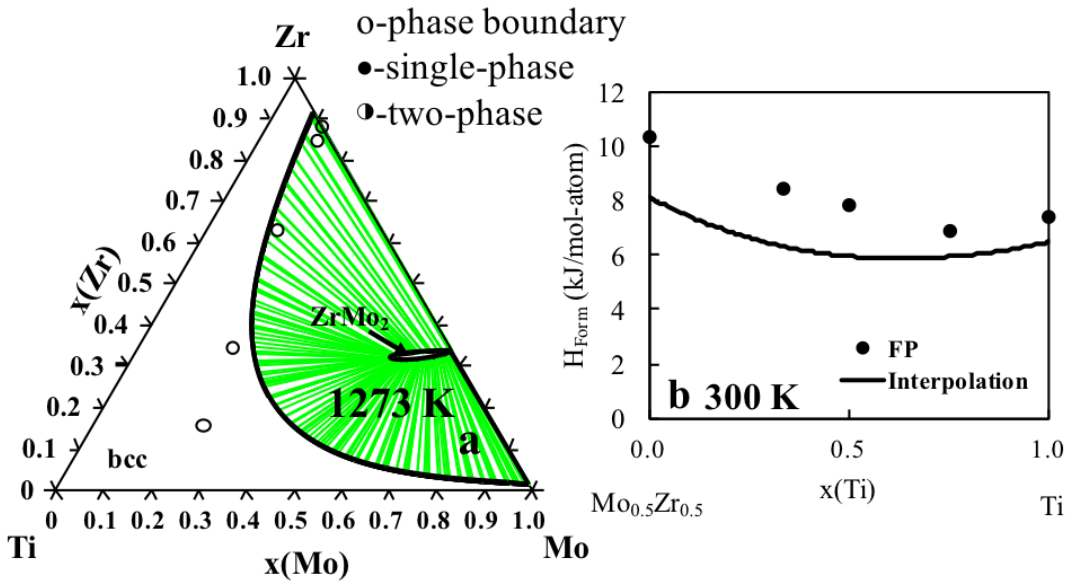


Figure 3.10: Binary interpolation of the isothermal section of the Ti-Mo-Zr system plotted at 1273 °K compared with experimental phase boundary data [24,25] (a), and enthalpy of formation of the bcc phase predicted by the previous thermodynamic modeling (solid line) at 300 °K versus the present first-principles calculations (circles) at 0 °K (b).

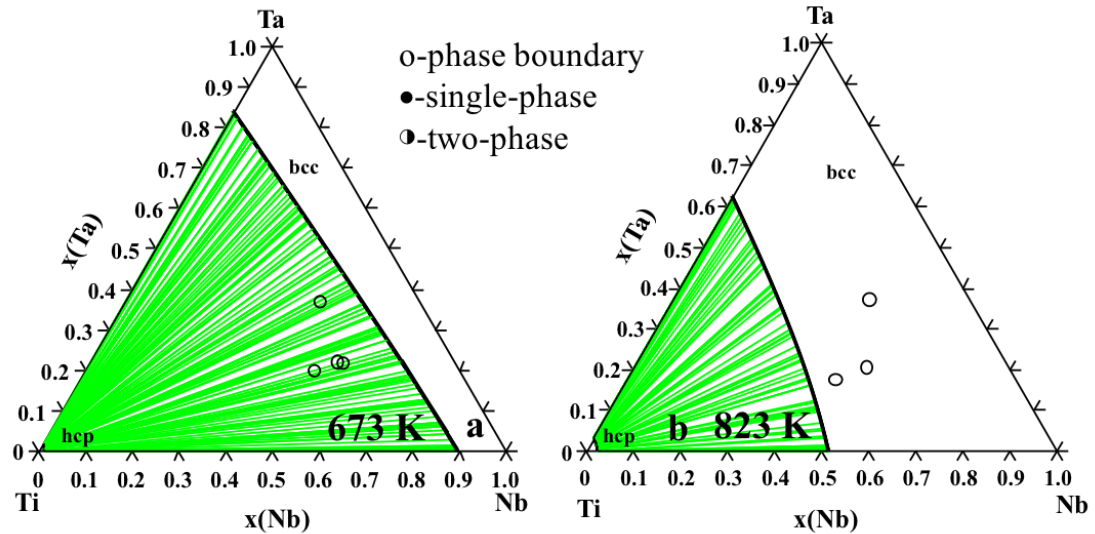


Figure 3.11: Binary interpolation of the isothermal section of the Ti-Nb-Ta system plotted at 673 °K compared with experimental phase boundary data [26] (a), and binary interpolation of the isothermal section of the Ti-Nb-Ta system plotted at 823 °K compared with experimental phase boundary data [26] (b).

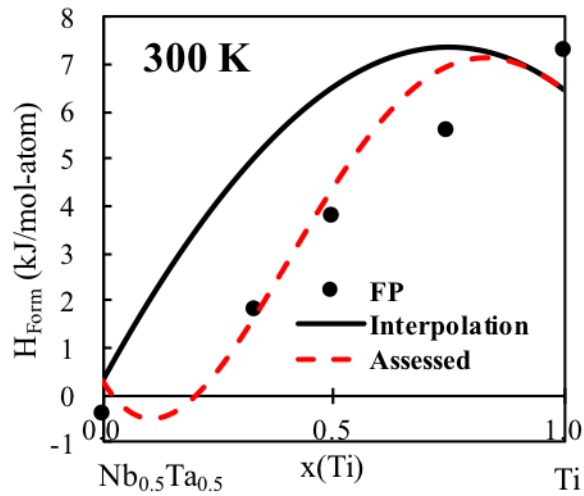


Figure 3.12: Enthalpy of formation of the bcc phase predicted by the previous thermodynamic modeling (solid line) at 300 °K and the ternary assessed thermodynamic modeling (red dotted line) versus the present first-principles calculations (circles) at 0 °K.

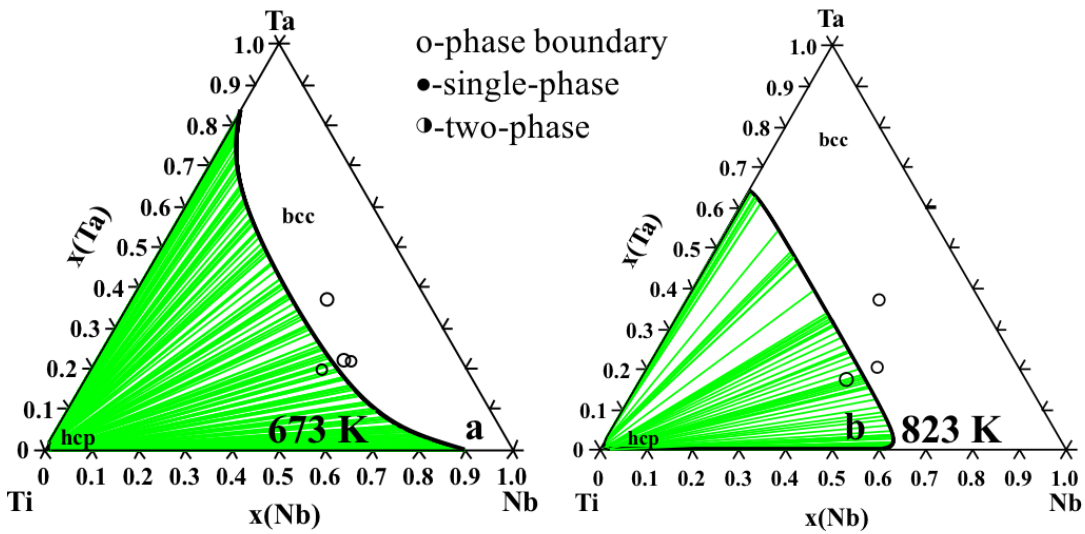


Figure 3.13: Ternary assessed isothermal section of the Ti-Nb-Ta system plotted at 673 °K compared with experimental phase boundary data [26] to ensure accuracy of the ternary assessment (a), and ternary assessed isothermal section at 823 °K compared with experimental phase boundary data [26] to ensure accuracy of the ternary assessment (b).

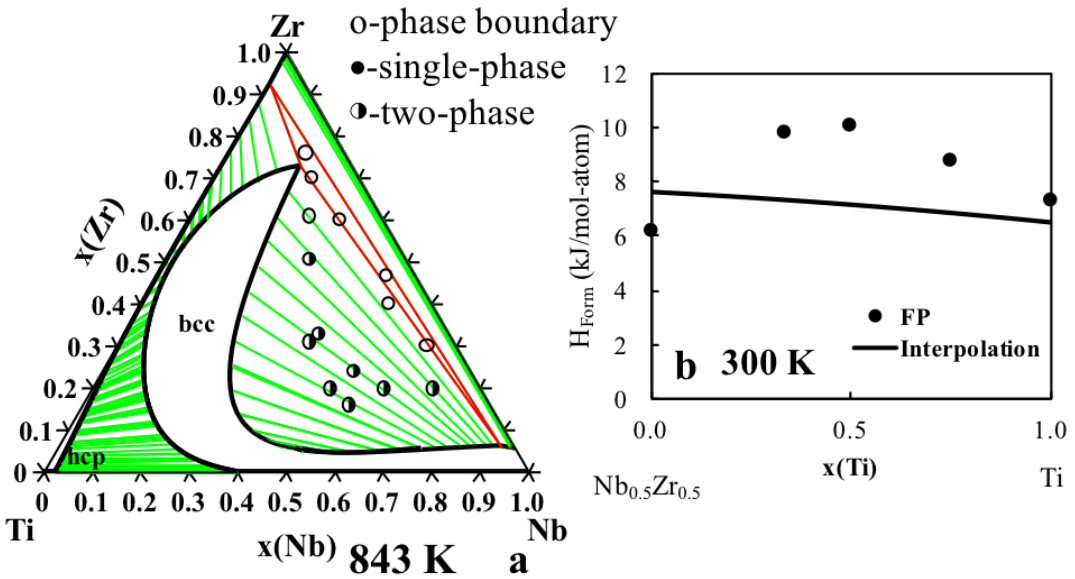


Figure 3.14: Binary interpolation of the isothermal section of the Ti-Nb-Zr system plotted at 843 °K compared with experimental phase boundary and two-phase region data [27] (a), and enthalpy of formation of the bcc phase predicted by the previous thermodynamic modeling (solid line) at 300 °K versus the present first-principles calculations (circles) at 0 °K (b).

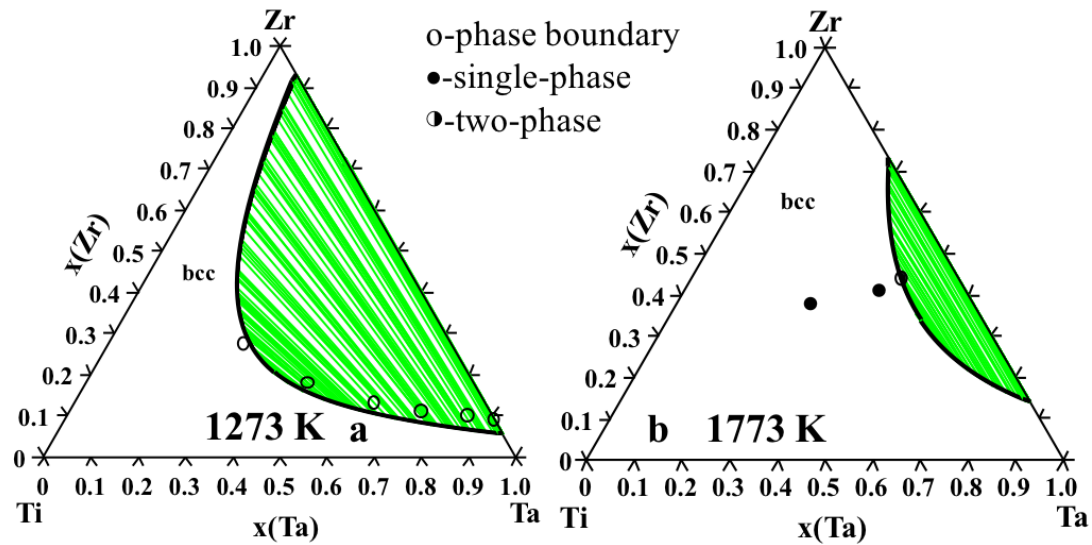


Figure 3.15: Binary interpolation of the isothermal section of the Ti-Ta-Zr system plotted at 1273 °K compared with experimental phase boundary data [28, 29] (a), and binary interpolation of the isothermal section of the Ti-Ta-Zr system plotted at 1773 °K compared with compared with experimental single phase and two-phase region data [28, 29] (b).

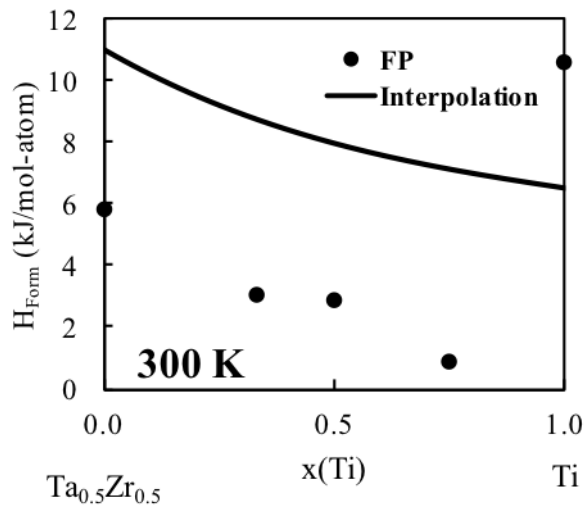


Figure 3.16: Enthalpy of formation of the bcc phase predicted by the previous thermodynamic modeling (solid line) at 300 °K versus the present first-principles calculations (circles) at 0 °K.

Chapter 6 |

Effects of alloying elements on the elastic properties of bcc ternary and higher ordered Ti-alloys

6.1 Introduction

In order to develop a better understanding about alloying effect on the elastic properties of Ti alloys, the present work is developing an elastic database for the Ti-Mo-Nb-Sn-Ta-Zr system. With the focus being on bcc Ti-alloys, the effects of alloying elements on the pure elements and Ti-X binary alloys in the bcc phase were calculated in chapter 5. After extrapolating to higher order systems, it was hypothesized that studying the effects of alloying on the elastic properties of ternary alloys would improve the database. The present work focuses on studying the elastic properties of the Ti-X-Y ($X \neq Y = Mo, Nb, Ta, Sn, and Zr$) ternary alloys in the bcc phase. The single crystal elastic stiffness constants (c_{ij} 's) and polycrystalline aggregate properties are predicted across the composition range using Density Functional Theory (DFT) at 0 °K outlined in the methodology chapter. Based on the DFT results, the CALPHAD approach outlined in the methodology is used to evaluate ternary interaction parameters. The interaction parameters are then incorporated into the database and the database accuracy is again tested similarly to the testing in chapter 5. The completed database is used to map the elastic modulus as a function of composition.

6.2 Modeling and Calculations

6.2.1 Calculation details

To study the elastic properties of the ternary bcc Ti alloys in the Ti-Mo-Nb-Sn-Ta-Zr system, DFT-based first-principles calculations were employed using the VASP (Vienna ab-initio simulation package) [61, 62]. Four kinds of calculations were performed for each ternary alloy Ti-X-Y, with the varying compositions of $X_{0.50}Y_{0.50}$ (16-atom supercell), $Ti_{0.33}X_{0.33}Y_{0.33}$ (36 atoms), $Ti_{0.50}X_{0.25}Y_{0.25}$ (32 atoms), $Ti_{0.74}X_{0.13}Y_{0.13}$ (64 atoms). The relaxation and use of SQS are discussed extensively in the methodology (chapter 2). The SQS used in this chapter were generated by Jiang et al. [73, 74]. The projector augmented wave (PAW) method was used to describe the ion-electron interaction. Based on our previous work done in chapter 5 (Figure 5.1), the X-C functional of the generalized gradient approximation depicted by Perdew, Burke, and Ernzerhof (PBE-GGA) [58] was employed. An energy cutoff roughly 1.3 times higher than the default values among all elements (i.e., 310 eV) was used for all calculations. The Brillouin zone sampling was done using the γ -centered Monkhorst-Pack scheme [91]. The k-point grids used for the ternary SQS were 4x4x4 and the k-point grids used for the binary $X_{0.50}Y_{0.50}$ SQS structures were an automated k-point mesh generator in VASP with the length of the subdivision specified at 80. The elastic calculations were completed using a strain magnitude of ± 0.01 based on the study done in chapter 5 and the results seen in Figure 5.2.

6.2.2 Modeling details

The first-principles results were then used to model the ternary interaction parameters of the elastic stiffness constants. The modeling was completed by plotting the binary interpolation from the working database build in chapter 5. The plots started at a 50-50 mixture ($X_{0.50}Y_{0.50}$) of the alloying elements ($X \neq Y = Mo, Nb, Sn, Ta, and Zr$) and plotted to pure Ti. The elastic stiffness constants of the pure elements and the binary interaction parameters from Table 5.2 were used to plot the binary interpolation. The differences between the ternary first-principles calculations and the binary interpolation were then used to obtain a single fitting parameter using the mathematica code in appendix C. With the focus being Ti-rich

alloys and wanting to follow the same modeling technique used on the binary alloys, the first-principles results with 70 at.% Ti or higher were weighted heavier (x6, according to the authors' practices) than the other points for the fittings. The best fit was found and the ternary interaction parameters were incorporated into the database. The databases was then used to predict the moduli values of the ternary and higher order alloys.

6.3 Results and discussion

6.3.1 Elastic calculation results

The elastic stiffness coefficients \bar{C}_{11} , \bar{C}_{12} , and \bar{C}_{44} are plotted in Figure 6.1 to Figure 6.6 for Ti-X-Y alloys ($X \neq Y = Mo, Nb, Sn, Ta, Zr$). The plots start from a 50-50 mixture of the alloying elements $X_{0.50}Y_{0.50}$ to Ti. The calculations are plotted as circles, the interpolation from the pure elements and binary interaction parameters is plotted as a red dashed line. The difference between the calculations and binary interpolation was used to fit the ternary interaction parameters. The ternary fitting is plotted as a solid black line. The calculated elastic stiffness coefficients are listed in Table 6.1.

The \bar{C}_{11} values, for most of the Ti-X-Y systems, decrease from $X_{0.50}Y_{0.50}$ to Ti (see Figure 6.1 and Figure 6.2). However, the Ti-Sn-Zr and Ti-Ta-Zr system differ. The \bar{C}_{11} values, for the Ti-Sn-Zr (Figure 6.2d), first increase from $Sn_{0.50}Zr_{0.50}$ to 60 at. % Ti and then decrease from 60 to 100 at. % Ti. The \bar{C}_{11} values, in the Ti-Ta-Zr system (Figure 6.2e), first increase from $Ta_{0.50}Zr_{0.50}$ to 35 at. % Ti and then decrease from 35 to 100 at. % Ti. The \bar{C}_{12} results are plotted in Figure 6.3 and Figure 6.4. The \bar{C}_{12} values decrease from $X_{0.50}Y_{0.50}$ to Ti, for the Ti-Mo-Nb, Ti-Mo-Ta and Ti-Nb-Ta systems. The \bar{C}_{12} values, for the Ti-Mo-Sn and Ti-Nb-Sn systems, first decrease from $X_{0.50}Y_{0.50}$ to 15 at. % Ti then increase from 15 to 85 at. % Ti and then decrease from 85 to 100 at. % Ti. The Ti-Mo-Zr and Ti-Nb-Zr systems show a decrease in \bar{C}_{12} value from $X_{0.50}Y_{0.50}$ to 60 at. % Ti and then an increase from 60 to 100 at. % Ti. The \bar{C}_{12} values increase from $X_{0.50}Y_{0.50}$ to 70 at. % Ti and then decrease from 70 to 100 at. % Ti for the Ti-Sn-Ta system. For the Ti-Sn-Zr system, the values increase from 0 to 100 at. % Ti and the \bar{C}_{12} values, for the Ti-Ta-Zr system, first decrease from 0 to 70 at. % Ti and then increase from 70

to 100 at. % Ti. The \bar{C}_{44} results are plotted in Figure 6.5 and Figure 6.6. The \bar{C}_{44} values decrease from $X_{0.50}Y_{0.50}$ to Ti, for the Ti-Mo-Sn and Ti-Ta-Zr systems. For the Ti-Mo-Zr and Ti-Mo-Ta systems, the \bar{C}_{44} values first decrease from 0 to 80 at. % Ti and then increase from 80 to 100 at. % Ti. The \bar{C}_{44} values, for the Ti-Mo-Nb and Ti-Nb-Ta systems, first decrease from $X_{0.50}Y_{0.50}$ to 65 at. % Ti and then increase from 65 to 100 at. % Ti. The \bar{C}_{44} values first increase from 0 to 80 at. % Ti and then decrease from 80 to 100 at. % Ti for the Ti-Nb-Sn and Ti-Nb-Zr systems. For the Ti-Sn-Ta system (Figure 6.6c), the values decrease from 0 until 20 at. % Ti, then increase from 20 to 50 at. % Ti and then decrease from 50 to 100 at. % Ti. The \bar{C}_{44} values, for the Ti-Sn-Zr system, first increase from $X_{0.50}Y_{0.50}$ to 60 at. % Ti and then decrease from 60 to 100 at. % Ti.

The trends in the ternary elastic stiffness coefficients can be summarized and explained by looking at the elastic stiffness calculations done on the pure elements and Ti-X ($X = \text{Mo, Nb, Sn, Ta, Zr}$) in chapter 5. The c_{11} and c_{12} of Mo, Nb and Ta are higher than Ti, while Sn and Zr are lower. The c_{44} for Mo and Ta are higher than Ti, while Nb, Sn, and Zr are lower. This can be explained because Mo, Nb and Ta are stable in the bcc structure at low temperatures while Ti, Sn and Zr are not, so the elastic stiffness coefficients are lower. The similarities of Mo, Nb and Ta are again noticed in the Ti-X data trends. The \bar{C}_{11} , \bar{C}_{12} , and \bar{C}_{44} all follow the same trends for the Ti-Mo, Ti-Nb, and Ti-Ta systems with the \bar{C}_{11} and \bar{C}_{12} increasing in value from 100 to 0 at. % Ti and the \bar{C}_{44} decreasing and then increasing from 100 to 0 at. % Ti. Based on this information, it is no surprise that the Ti-Mo-Nb, Ti-Mo-Ta and Ti-Nb-Ta systems have the same trends in their c_{ij} data. When Ti-Mo, Ti-Nb, and Ti-Ta are alloyed with Sn in the ternary systems, they show similar trends for the most, not all, of the c_{ij} . The same is true for the Ti-Mo, Ti-Nb, and Ti-Ta systems alloyed with Zr.

Based on the discussion in the methodology, Born's criteria is used to look at the mechanical stability of the bcc phase. When $\bar{C}_{11}-\bar{C}_{12}$ becomes negative then the bcc phase loses mechanical stability and is thus plotted in Figure 6.7. Based on the present results, the bcc phase loses mechanical stability in the Ti-Mo-Nb, Ti-Mo-Ta, Ti-Mo-Zr, Ti-Nb-Zr, Ti-Sn-Zr, and Ti-Ta-Zr systems when the Ti concentration is more than 90 at. %, with the values being 91, 92, 95, 93, 91, and 94 at. % Ti, respectively. The bcc phase loses mechanical stability at Ti concentrations above 87, 77, 89, and 80 at. % Ti for Ti-Mo-Sn, Ti-Nb-Sn, Ti-Nb-Ta and Ti-Sn-Ta systems,

respectively. Close to where the bcc phase loses its mechanical stability, the Young's modulus is reduced and such compositions may be desirable low modulus bcc Ti alloys. As discussed above, Mo, Nb and Ta are strong β -stabilizers and thus the Ti-Mo-Nb, Ti-Mo-Ta, and Ti-Nb-Ta systems stabilize the bcc phase similarly. Also, discussed previously, Zr is a weak β -stabilizer alone but when alloyed with other elements it acts a strong α -stabilizer. This is observed with these results with the Ti-Mo-Zr, Ti-Nb-Zr, Ti-Ta-Zr systems all stabilizing the bcc phase at high Ti concentrations (95, 93, and 94 at. % respectively). Zr is even able to stabilize the Ti-Sn-Zr system at a high Ti concentration of 91 at. % Ti, even with Sn. Sn is not stable in the bcc phase and is not a β -stabilizer. So, when alloyed with Sn, a higher concentration of other alloying elements is needed to stabilize the bcc phase.

Figure 6.8 and Figure 6.9 plot the Young's moduli (E) calculations (circles) for each Ti-X-Y ternary system ($X \neq Y = \text{Mo, Nb, Sn, Ta, Zr}$) starting from a 50-50 mixture of the two alloying elements to Ti. The red dashed line is the average from the Hill approach interpolated from the binary interaction parameters shown in Table 6.3. The average from the Hill approach (black solid line), Voigt (purple dotted line), Reuss (gold dotted-dashed line) bounds are plotted using the binary and ternary interaction parameters. The Voigt and Reuss bounds vary more drastically when the bcc structure is unstable as opposed to when the bcc structure is stable. The average from the Hill approach using the binary and ternary interaction parameters is what the database predicts because it has been shown to be a more accurate representation of the Young's modulus than the Voigt or Reuss approximations [70, 111]. Whenever possible experimentally determined Young's moduli [38–41] (data listed in Table 6.2) are plotted for comparison. The difference/error between the previous results (both experimental and from calculations) and the present first-principles results are calculated by Eq. 2.30.

The first-principles E , for the Ti-Mo-Nb (Figure 6.8a) system are compared with experimentally obtained E data in the review paper by Niinomi et al. [40]. The experimental E results were obtained using a nanoindenter after solution treatment. The experimental E values are higher than the Hill average calculated values (difference of 71 GPa or an error of 0.65 using Eq. 2.30) and more closely match the Voigt bound (difference of 46 GPa). Niinomi [40] pointed out that Young's moduli obtained from the microhardness testing are higher than the polycrystalline Young's moduli value, thus our calculation results should be close to the polycrystalline E

values. The present data show that the E decreases in value from 0 to 100 at. % Ti.

In the literature, no bcc Ti-Mo-Sn (Figure 6.8b) experimental E results were found to be compared with the present work. The Voigt-Reuss bounds and the Hill average are quite similar until around 65 at. % Ti when they begin to vary. The E values decrease from 0 to 100 at. % Ti. The calculated E results for the Ti-Mo-Ta alloy system (Figure 6.9c) are compared with experimental data reported by Niinomi et al. [40] and Mohammed et al. [39]. The E values reported by Niinomi et al. [40] were obtained using an ultrasonic measurement after the samples were solution treated. Niinomi et al. [40] pointed out that E values obtained using the ultrasonic method obtained normally fall in between the E values determined using tensile testing or microhardness testing. Niinomi et al. [40] also showed that when multiple authors test the same composition alloy using the ultrasonic technique their answers vary less drastically than when multiple authors test the same compositions using tensile or microhardness. The experimental E fit well with the present Voigt bound (difference of 9 GPa) and had an error of 0.46 (Eq. 2.30) from the Hill average (difference of 33 GPa). The E values decrease from 0 to 100 at. % Ti.

The calculated E of the Ti-Mo-Zr alloy system (Figure 6.8d) is compared with experimental values reported by Mohammed et al. [39]. The error in the experiments and methodology was not discussed. The experimental E [39] and the present E (Hill average) vary by less than 6 GPa and the E values decrease from 0 to 100 at. % Ti. Experimentally determined Young's moduli results from Niinomi et al. [40], Mohammed et al. [39], and Nozoe et al. [41] are compared with the present E calculations for the Ti-Nb-Sn alloy system (Figure 6.8e). The experimental E results reported by Niinomi et al. [40] were obtained through tensile testing of samples that were solution treated and cold rolled. Niinomi et al. showed that E results at this specific composition varied by 10 GPa. The E results reported by Niinomi et al. [40] and Mohammed et al. [39] differ from the Hill average by 9 and 15 GPa, respectively (an error of 0.28 using Eq. 2.30). The E results from Nozoe et al. [41] differ by 10, 32 and 78 GPa from the Voigt, Hill and Reuss results, respectively, and have an error of 0.56 (Eq. 2.30). However, Nozoe et al. reported that the samples formed the metastable ω phase. The ω phase is a metastable hexagonal phase (space group P6/mmm) with lattice parameters closely

matching those of the bcc phase. Nozoe et al. [41] also discussed how the aging of the Ti-Mo-Sn samples greatly affected the E . The E values, for the Ti-Nb-Sn system, increase from 0 to 35 at. %Ti and then decrease from 35 to 100 at. %Ti. So overall the calculations satisfactorily predicted the Young's moduli of the Ti-Mo-Nb, Ti-Mo-Sn, Ti-Mo-Ta, Ti-Mo-Zr and Ti-Nb-Sn systems.

Figure 6.9 continues to plot the E of the Ti-X-Y ternary alloy systems. The first-principles E , for the Ti-Nb-Ta system, are compared with experimentally determined E values reported by Mohammed et al. [39] (Figure 6.9a). At this composition, the Voigt and Reuss bounds are very close to the Hill average. Thus, while the experimental E result fits closer to the Reuss bound (difference of 8 GPa), the experimental E result only varies by 15 and 21 GPa from the Hill and Voigt results, respectively and has an error of 0.28 (Eq. 2.30). Niinomi et al. [40] reported E values for the Ti-Nb-Ta system. However, the experimental values at the same compositions varied by more than 40 GPa and thus his results were not plotted for comparison here. The E decreases in value from 0 to 100 at. % Ti in the Ti-Nb-Ta ternary system.

The first-principles E results for the Ti-Nb-Zr (Figure 6.9b) system are compared with experimentally determined E results from Geetha et al. [38], Mohammed et al. [39], and Niinomi et al. [40]. The experimental E results reported by Niinomi et al. [40] are for the Ti-13Nb-13Zr and Ti-27Nb-8Zr alloys. The results for the Ti-13Nb-13Zr were obtained using both the ultrasonic and 3-point bending tests and varied by 50 GPa, while the Ti-27Nb-8Zr results were obtained using tensile testing and varied by 50 GPa. The experimentally determined E results varied from the present Voigt, Hill and Reuss results by an average of 9, 2, and 14 GPa, respectively and has an error of 0.08 (Eq. 2.30) from the Hill average. The E values first increase from 0 to 70 at. % Ti and then decrease from 70 to 100 at. % Ti, for the Ti-Nb-Zr system. The Ti-Sn-Ta, Ti-Sn-Zr and Ti-Ta-Zr alloy systems did not have experimental data to be compared with and our results are shown in Figure 6.9c, Figure 6.9d, and Figure 6.9e, respectively. For the Ti-Sn-Ta system, the E values decrease from 0 to 100 at. % Ti. The E values, for the Ti-Sn-Zr system, first increase from 0 to 60 at. % Ti and then decrease from 60 to 100 at. % Ti. The E values for the Ti-Ta-Zr system first decrease from 0 to 15 at. % Ti, where the values begin to increase from 15 to 30 at. % Ti and then decrease from 30 to 100 at. % Ti.

The first-principles calculations and the CALPHAD fittings are done using data obtained at 0 °K while the experiments are obtained using polycrystalline samples at 300 °K. Considering this and the fact that the experimental measured E values vary at the same composition, the experimental values fit well within the bounds set by Reuss and Voigt, and the Hill average generally reproduces the experimentally determined E data for the Ti-X-Y ternary alloys.

Using the complete database with interaction parameters listed in Table 5.2, the elastic stiffness coefficients can be predicted and then the moduli values can be calculated and mapped. Figure 6.10 and Figure 6.11 uses the global minimization tools in pycalphad [42] to map the E based on composition for Ti-X-Y ternaries. The ternary maps all have regions in the Ti rich corner that are light blue indicating that the Young's moduli are low enough to be in the target E range. With this fact and the fact that six of the Ti-X-Y ternaries all stabilize the bcc phase above 90 at. % Ti, the database points to multiple composition ranges that would yield possible implant materials. The pycalphad code and completed database used are in appendix D and E.

The B and G moduli calculated (circles) are plotted in Figures 6.12-6.15 for each Ti-X-Y ($X \neq Y = \text{Mo, Nb, Sn, Ta, Zr}$) system starting from a 50-50 mixture of X and Y to Ti. The red dashed line is the Hill average interpolated from the binary interaction parameters shown in Table 6.3. The Hill average (black solid line), Voigt (purple dotted line), Reuss (gold dotted-dashed line) bounds are plotted using the binary and ternary interaction parameters and listed in Table 6.2. The B values, for all the Ti-X-Y ternaries except Ti-Nb-Sn, Ti-Sn-Ta and Ti-Sn-Zr decrease from 0 to 100 at. % Ti, as shown in Figure 6.12 and Figure 6.13. The B values for the Ti-Nb-Sn and Ti-Sn-Ta systems first decrease from 0 to 10 at. % Ti and then increase from 10 to 55 at. % Ti and then decrease from 55 to 100 at. % Ti. For the Ti-Sn-Zr system, the B values first increase from 0 to 85 at. % Ti and then decrease from 85 to 100 at. % Ti. The G values decrease from 0 to 100 at. % Ti for all the ternary systems except Ti-Nb-Sn, Ti-Nb-Zr, Ti-Sn-Zr and Ti-Ta-Zr (Figure 6.14 and Figure 6.15). The G values increase from 0 to 60 at. % Ti and then decrease from 60 to 100 at. % Ti for the Ti-Nb-Sn, Ti-Nb-Zr systems. For the Ti-Sn-Zr system, the G values first increase from 0 to 55 at. % Ti and then decrease from 55 to 100 at. % Ti. The G values increase from 0 to 40 at. % Ti and then decrease from 40 to 100 at. % Ti for the Ti-Ta-Zr system.

The B and G moduli calculated (circles) are plotted in Figure 6.12 to Figure 6.15 for each Ti-X-Y ($X \neq Y = \text{Mo, Nb, Sn, Ta, Zr}$) system starting from a 50-50 mixture of X and Y to Ti. The red dashed line is the Hill average interpolated from the binary interaction parameters shown in Table 5.2. The Hill average (black solid line), Voigt (purple dotted line), Reuss (gold dotted-dashed line) bounds are plotted using the binary and ternary interaction parameters (Table 5.2 and 6.3). The B values, for all the Ti-X-Y ternaries except Ti-Nb-Sn, Ti-Sn-Ta and Ti-Sn-Zr decreases from 0 to 100 at.% Ti, as shown in Figure 6.12 and Figure 6.13. The B values for the Ti-Nb-Sn and Ti-Sn-Ta systems first decrease from 0 to 10 at.% Ti and then increase from 10 to 55 at.% Ti and then decrease from 55 to 100 at.% Ti. For the Ti-Sn-Zr system, the B values first increase from 0 to 85 at.% Ti and then decreases from 85 to 100 at.% Ti. The G values decrease from 0 to 100 at.% Ti for all the ternary systems except Ti-Nb-Sn, Ti-Nb-Zr, Ti-Sn-Zr and Ti-Ta-Zr (Figure 6.14 and Figure 6.15). The G values increase from 0 to 60 at.% Ti and then decrease from 60 to 100 at.% Ti for the Ti-Nb-Sn, Ti-Nb-Zr systems. For the Ti-Sn-Zr system, the G values first increase from 0 to 55 at.% Ti and then decrease from 55 to 100 at.% Ti. The G values increase from 0 to 40 at.% Ti and then decrease from 40 to 100 at.% Ti for the Ti-Ta-Zr system.

Both the G and E are negative when they are close to Ti. This is due to the instability of the bcc phase close to Ti. As discussed by BornâŽs criteria, when $\bar{C}_{11}-\bar{C}_{12}$ is negative the bcc phase loses mechanical stability. The Voigt bound of G_v is expressed by:

$$G_v = (\bar{C}_{11} - \bar{C}_{12} + \bar{C}_{44}) / 5 \quad (6.1)$$

So, when $\bar{C}_{11}-\bar{C}_{12}$ is negative, it can cause G to be negative. The E is then calculated from the B and G , so when G is negative it can cause E to be negative. This is one of the reasons that finding bcc Ti alloys close to the bcc stability will produce a low E .

6.3.2 Extrapolation to higher ordered systems

The Young's moduli are predicted and compared with experimental results for higher order Ti alloys and the results are shown in Table 6.4 and Figure 6.16. The same comparison was made in chapter 5, but those predictions were made

without the ternary interaction parameters. Figure 6.16 plots the calculated Young's moduli (Hill average) versus the experimentally determined Young's moduli [37–39]. The black diagonal line would be a perfect correlation between the predictions and experiments. The grey region is the average variance in the first-principles calculations when calculating the average elastic stiffness coefficients using Eq. 2.18–Eq. 2.20 (3 GPa). The same higher order alloys were picked to compare the effect of introducing the ternary interaction parameters. As discussed previously, the error bars plotted for the experiments come from the variance that was seen when comparing the experimentally determined Young's moduli at the same composition from Niinomi et al. [40], Geetha et al. [38], Tane et al. [37], and Mohammed et al. [39]. The horizontal error bars are the Voigt and Reuss bounds. Previously, without ternary interaction parameters, the predictions and experimental results varied anywhere between 0.69 and 14 GPa and on average by 7 GPa. The calculations are usually larger than the experimental values due to the temperature difference: the computed single crystal elastic stiffness coefficients are at 0 °K, while the experiments on the polycrystalline samples are usually performed at 300 °K. As expected, introducing ternary interaction parameters improves the database. The introduction of the ternary interaction parameters improved the predictions to vary anywhere from 0.39 to 13 GPa from the experimental values with an average variance of only 5 GPa. Thus, while the ternary interactions have small effects on the final results, the introduction of Ti-containing ternary interaction parameters still improves the predictions and the database is more accurate to predict the Young's moduli of higher order Ti alloys.

6.4 Conclusion

The present study systematically calculated the elastic properties of the bcc Ti ternary alloys, including the elastic stiffness constants, bulk modulus, shear modulus, and Young's modulus. Five alloying elements, Mo, Nb, Sn, Ta and Zr were studied. The general CALPHAD modeling approach was used to fit ternary interaction parameters. From the elastic stiffness constant data, the Ti-X-Y ($X \neq Y = Mo, Nb, Ta$) showed the same trends in the data. This is to be expected because Mo, Nb, and Ta are similar elements that are strong β -stabilizers and stable in the bcc phase at low temperatures. It was also seen that the Ti-X-Sn ($X = Mo, Nb, Ta$)

alloys showed similar trends in the data for most of the elastic stiffness constants, so did the Ti-X-Zr (X = Mo, Nb, Ta) alloys. The present calculations showed that the bcc Ti-alloy was mechanically stabilized at compositions less than 91, 92, 95, 93, 91, 94, 87, 77, 89, and 80 at % Ti for the Ti-Mo-Nb, Ti-Mo-Ta, Ti-Mo-Zr, Ti-Nb-Zr, Ti-Sn-Zr, Ti-Ta-Zr, Ti-Mo-Sn, Ti-Nb-Sn, Ti-Nb-Ta and Ti-Sn-Ta alloys, respectively. As discussed above, Mo, Nb and Ta are strong β -stabilizers and thus the Ti-Mo-Nb, Ti-Mo-Ta, and Ti-Nb-Ta systems stabilize the bcc phase similarly. Also, discussed previously, Zr is a weak β -stabilizer alone but when alloyed with other elements it acts a strong β -stabilizer. This was observed with the Ti-Mo-Zr, Ti-Nb-Zr, Ti-Ta-Zr systems all stabilizing the bcc phase at high Ti concentrations (95, 93, and 94 at.% respectively). Zr was even able to stabilize the Ti-Sn-Zr system at a high Ti concentration of 91 at.% Ti, even with Sn not being a *beta*-stabilizer or stable in the bcc phase.

The pure element elastic results along with the binary and ternary interaction parameters were combined into a database file in appendix D. The database was used to map possible alloy compositions to find potential materials with a Young's modulus in the target range for biomedical load-bearing implants using the pycalphd code in appendix E. Overall, the introduction of the ternary interaction parameters improved the database's ability to predict the E of higher order alloys by a small amount. The complete database satisfactorily predicts the elastic properties of higher order Ti-alloys and will help guide future research to develop low-modulus biocompatible Ti alloys.

Table 6.1: First-principles calculations of the elastic stiffness constants for different atomic percent compositions of the bcc Ti-X-Y ternary systems at 0 °K

Reference	$Ti_{1-bc}X_bY_c$	\overline{C}_{11}	\overline{C}_{11}	\overline{C}_{11}
This work	Ti	93	115	41
This work	$Ti_{0.74}Mo_{0.13}Nb_{0.13}$	155	121 ± 4	34 ± 4
This work	$Ti_{0.50}Mo_{0.25}Nb_{0.25}$	222 ± 3	129 ± 3	33 ± 3
This work	$Ti_{0.33}Mo_{0.33}Nb_{0.33}$	269 ± 5	134 ± 3	42 ± 4
This work	$Mo_{0.50}Nb_{0.50}$	414 ± 6	165 ± 3	68
This work	$Ti_{0.74}Mo_{0.13}Sn_{0.13}$	137 ± 15	121 ± 2	56 ± 13
This work	$Ti_{0.50}Mo_{0.25}Sn_{0.250}$	160 ± 3	130 ± 8	71 ± 2
This work	$Ti_{0.33}Mo_{0.33}Sn_{0.33}$	167 ± 8	133 ± 6	75 ± 2
This work	$Mo_{0.50}Sn_{0.50}$	192 ± 28	130 ± 36	40 ± 31
This work	$Ti_{0.74}Mo_{0.13}Ta_{0.13}$	153 ± 1	125 ± 4	38 ± 3
This work	$Ti_{0.50}Mo_{0.25}Ta_{0.25}$	222 ± 2	136 ± 1	45 ± 3
This work	$Ti_{0.33}Mo_{0.33}Ta_{0.33}$	263 ± 4	145 ± 6	49 ± 4
This work	$Mo_{0.50}Ta_{0.50}$	370 ± 13	163 ± 4	63 ± 4
This work	$Ti_{0.74}Mo_{0.13}Zr_{0.13}$	125 ± 1	109 ± 8	35 ± 1
This work	$Ti_{0.50}Mo_{0.25}Zr_{0.25}$	160 ± 1	116 ± 5	34 ± 2
This work	$Ti_{0.33}Mo_{0.33}Zr_{0.33}$	182 ± 1	116 ± 2	31 ± 8
This work	$Mo_{0.50}Zr_{0.50}$	231 ± 7	118 ± 5	33 ± 8
This work	$Ti_{0.74}Nb_{0.13}Sn_{0.13}$	115 ± 4	118 ± 3	55
This work	$Ti_{0.50}Nb_{0.25}Sn_{0.25}$	131 ± 9	121 ± 6	64 ± 3
This work	$Ti_{0.33}Nb_{0.33}Sn_{0.33}$	134 ± 2	122 ± 3	67 ± 6
This work	$Nb_{0.50}Sn_{0.50}$	132 ± 4	118 ± 8	56 ± 4
This work	$Ti_{0.74}Nb_{0.13}Ta_{0.13}$	130 ± 3	124 ± 4	37 ± 3
This work	$Ti_{0.50}Nb_{0.25}Ta_{0.25}$	182 ± 1	129 ± 4	43 ± 6
This work	$Ti_{0.33}Nb_{0.33}Ta_{0.33}$	208	135 ± 1	44 ± 1
This work	$Nb_{0.50}Ta_{0.50}$	260 ± 2	148 ± 3	47 ± 3
This work	$Ti_{0.74}Nb_{0.13}Zr_{0.13}$	101 ± 2	113 ± 4	32 ± 3
This work	$Ti_{0.50}Nb_{0.25}Zr_{0.25}$	122 ± 1	113 ± 3	28 ± 3
This work	$Ti_{0.33}Nb_{0.33}Zr_{0.33}$	143 ± 2	107 ± 5	28 ± 3
This work	$Nb_{0.50}Zr_{0.50}$	154 ± 5	110 ± 3	15 ± 2
This work	$Ti_{0.74}Sn_{0.13}Ta_{0.13}$	115 ± 6	121 ± 4	60 ± 2

Table 6.1: First-principles calculations of the elastic stiffness constants for different atomic percent compositions of the bcc Ti-X-Y ternary systems at 0 °K

Reference	$Ti_{1-bc}X_bY_c$	\overline{C}_{11}	\overline{C}_{11}	\overline{C}_{11}
This work	$Ti_{0.50}Sn_{0.25}Ta_{0.25}$	138 ± 13	125 ± 4	75 ± 4
This work	$Ti_{0.33}Sn_{0.33}Ta_{0.33}$	138 ± 6	131 ± 8	78 ± 1
This work	$Sn_{0.50}Ta_{0.50}$	133 ± 8	130 ± 4	60 ± 4
This work	$Ti_{0.74}Sn_{0.13}Zr_{0.13}$	97 ± 5	111 ± 4	55 ± 2
This work	$Ti_{0.50}Sn_{0.25}Zr_{0.25}$	99 ± 12	103 ± 4	59 ± 7
This work	$Ti_{0.33}Sn_{0.33}Zr_{0.33}$	96 ± 7	98 ± 3	55 ± 3
This work	$Sn_{0.50}Zr_{0.50}$	85 ± 7	87 ± 9	42 ± 3
This work	$Ti_{0.74}Ta_{0.13}Zr_{0.13}$	136 ± 36	103 ± 21	44 ± 5
This work	$Ti_{0.50}Ta_{0.25}Zr_{0.25}$	130 ± 3	117 ± 4	42 ± 7
This work	$Ti_{0.33}Ta_{0.33}Zr_{0.33}$	148 ± 1	115 ± 2	44 ± 2
This work	$Ta_{0.50}Zr_{0.50}$	157 ± 2	123 ± 3	35 ± 3

Table 6.2: First-principles calculations of the bulk modulus B , shear modulus G , and Young's modulus E in GPa for different atomic percent compositions of the bcc Ti-X-Y ternary systems at 0 °K as well as experimental data obtained for the Young's modulus at 300 °K by the references stated.

Reference	Ti _{100-2b} X _b Y _b	B	G	E
This work	Ti	108	-12.91	-40.34
This work	TiMo _{12.5} Nb _{12.5}	132 ±4	26 ±4	73 ±4
This work	TiMo _{25.0} Nb _{25.0}	160 ±3	38 ±3	105 ±3
This work	TiMo _{33.3} Nb _{33.3}	179 ±5	51 ±5	139 ±5
This work	Mo ₅₀ Nb ₅₀	248 ±6	87 ±6	233 ±6
Expt 300 K [40]	TiMo ₆ Nb ₂			110
This work	TiMo _{12.5} Sn _{12.5}	126 ±15	27 ±15	75 ±15
This work	TiMo _{25.0} Sn _{25.0}	140 ±8	39 ±8	106 ±8
This work	TiMo _{33.3} Sn _{33.3}	144 ±8	42 ±8	114 ±8
This work	Mo ₅₀ Sn ₅₀	151 ±36	36 ±36	100 ±36
This work	TiMo _{12.5} Ta _{12.5}	134 ±4	25 ±4	72 ±4
This work	TiMo _{25.0} Ta _{25.0}	165 ±2	44 ±3	122 ±3
This work	TiMo _{33.3} Ta _{33.3}	184 ±6	53 ±6	145 ±
This work	Mo ₅₀ Ta ₅₀	232 ±13	77 ±13	208 ±13
Expt 300 K [39]	TiMo ₇ Ta ₁			74
Expt 300 K [40]	TiMo ₇ Ta ₁			74
This work	TiMo _{12.5} Zr _{12.5}	114 ±8	20 ±8	55 ±8
This work	TiMo _{25.0} Zr _{25.0}	131 ±5	29 ±5	80 ±5
This work	TiMo _{33.3} Zr _{33.3}	138 ±2	32 ±8	89 ±8
This work	Mo ₅₀ Zr ₅₀	156 ±7	41 ±8	113 ±8
Expt 300 K [39]	TiMo ₇ Zr ₃			64
This work	TiNb _{12.5} Sn _{12.5}	117 ±4	14 ±4	41 ±4
This work	TiNb _{25.0} Sn _{25.0}	124 ±9	26 ±9	72 ±9
This work	TiNb _{33.3} Sn _{33.3}	126 ±6	28 ±6	78 ±6
This work	Nb ₅₀ Sn ₅₀	123 ±8	26 ±8	72 ±8
Expt 300 K [39]	TiNb ₂₂ Sn ₂			44
Expt 300 K [40]	TiNb ₂₂ Sn ₂			50
Expt 300 K [41]	TiNb ₉ Sn ₃			58
This work	TiNb _{12.5} Ta _{12.5}	126 ±4	15 ±4	43 ±4

Table 6.2: First-principles calculations of the bulk modulus B , shear modulus G , and Young's modulus E in GPa for different atomic percent compositions of the bcc Ti-X-Y ternary systems at 0 °K as well as experimental data obtained for the Young's modulus at 300 °K by the references stated.

Reference	$\text{Ti}_{100-2b}X_b\text{Y}_b$	B	G	E
This work	$\text{TiNb}_{25.0}\text{Ta}_{25.0}$	147 ±6	35 ±6	98 ±6
This work	$_{33.3}\text{Ta}_{33.3}$	159 ±1	41 ±1	113 ±1
This work	$\text{Nb}_{50}\text{Ta}_{50}$	185 ±3	50 ±3	140 ±3
Expt 300 K [39]	$\text{TiNb}_{10}\text{Ta}_{19}$			55
This work	$\text{TiNb}_{12.5}\text{Zr}_{12.5}$	109 ±4	-2 ±4	-6 ±4
This work	$\text{TiNb}_{25.0}\text{Zr}_{25.0}$	116 ±3	14 ±3	40 ±3
This work	$\text{TiNb}_{33.3}\text{Zr}_{33.3}$	119 ±5	23 ±5	66 ±5
This work	$\text{Nb}_{50}\text{Zr}_{50}$	125 ±5	17 ±5	50 ±5
Expt 300 K [39]	TiNb_8Zr_8			77
Expt 300 K [39]	$\text{TiNb}_{12}\text{Zr}_9$			14
Expt 300 K [39]	$\text{TiNb}_{11}\text{Zr}_3$			50
Expt 300 K [40]	$\text{TiNb}_{17}\text{Zr}_5$			78
Expt 300 K [38]	TiNb_8Zr_8			81
This work	$\text{TiSn}_{12.5}\text{Ta}_{12.5}$	119 ±6	13 ±6	39 ±6
This work	$\text{TiSn}_{25.0}\text{Ta}_{25.0}$	129 ±13	31 ±13	86 ±13
This work	$\text{TiSn}_{33.3}\text{Ta}_{33.3}$	133 ±8	28 ±8	79 ±8
This work	$\text{Sn}_{50}\text{Ta}_{50}$	131 ±8	20 ±8	57 ±8
This work	$\text{TiSn}_{12.5}\text{Zr}_{12.5}$	106 ±5	4 ±5	13 ±5
This work	$\text{TiSn}_{25.0}\text{Zr}_{25.0}$	102 ±12	15 ±12	42 ±12
This work	$\text{TiSn}_{33.3}\text{Zr}_{33.3}$	97 ±7	15 ±7	43 ±7
This work	$\text{Sn}_{50}\text{Zr}_{50}$	86 ±9	11 ±9	32 ±9
This work	$\text{TiTa}_{12.5}\text{Zr}_{12.5}$	114 ±21	30 ±21	82 ±21
This work	$\text{TiTa}_{25.0}\text{Zr}_{25.0}$	121 ±4	20 ±7	58 ±7
This work	$\text{TiTa}_{33.3}\text{Zr}_{33.3}$	126 ±2	30 ±2	83 ±2
This work	$\text{Ta}_{50}\text{Zr}_{50}$	134 ±3	26 ±3	74 ±3

Table 6.3: Evaluated interactions parameters (L_2 , Eq. 2.30) for the elastic stiffness constants of the Ti-containing ternary alloys.

Alloy	Interaction Parameter	\overline{C}_{11}	\overline{C}_{12}	\overline{C}_{44}
Ti-Mo-Nb	L_2	-29.97	13.97	9.72
Ti-Mo-Sn	L_2	-83.85	31.80	74.73
Ti-Mo-Ta	L_2	-106.53	-12.35	5.27
Ti-Mo-Zr	L_2	-245.27	50.43	-44.96
Ti-Nb-Sn	L_2	-41.52	25.52	67.85
Ti-Nb-Ta	L_2	-93.77	-15.80	4.25
Ti-Nb-Zr	L_2	-220.35	72.10	-55.29
Ti-Sn-Ta	L_2	-95.39	-10.94	67.85
Ti-Sn-Zr	L_2	-155.34	68.86	3.85
Ti-Ta-Zr	L_2	-149.67	-8.91	-23.70

Table 6.4: Predicted Young's moduli (E) (in GPa) of higher order alloys using the binary and ternary interaction parameters in the bcc phase compared to the predicted Young's moduli (E_{BIN}) using just the binary interaction parameters and the experimental values found with both the weight percent and atomic percent listed.

Alloy Name (%wt)	at %	Calc E_{BIN}	Calc E	Expt E
Ti-35Nb-7Zr-5Ta [38]	Ti-24Nb-5Zr-2Ta	81	78	80
Ti-29Nb-13Ta-4.6Zr [38]	Ti-20Nb-5Ta-3Zr	76	73	75
Ti-29Nb-13Ta-6Sn [38]	Ti-21Nb-5Ta-3Sn	68	68	74
Ti-29Nb-13Ta-4.6Sn [38]	Ti-20Nb-5Ta-3Sn	67	66	66
Ti-29Nb-13Ta-4.5Zr [38]	Ti-20Nb-5Ta-3Zr	76	73	65
Ti-29Nb-13Ta-4.6Zr [37]	Ti-21Nb-5Ta-3Zr	76	75	64
Ti-30Nb-10Ta-5Zr [37]	Ti-23Nb-4Ta-3Zr	77	74	64
Ti-35Nb-10Ta-5Zr [37]	Ti-25Nb-4Ta-4Zr	80	78	65
Ti-24Nb-4Zr-7.9Sn [39]	Ti-15Nb-3Zr-4Sn	65	62	54
Ti-35Nb-2Ta-3Zr [39]	Ti-23Nb-1Ta-2Zr	69	68	61
Ti-29Nb-11Ta-5Zr [39]	Ti-20Nb-6Ta-2Zr	74	72	60
Ti-10Zr-5Ta-5Nb [39]	Ti-6Zr-1Ta-3Nb	64	62	52
Ti-29Nb-13Ta-2Sn [39]	Ti-20Nb-5Ta-1Sn	66	65	62

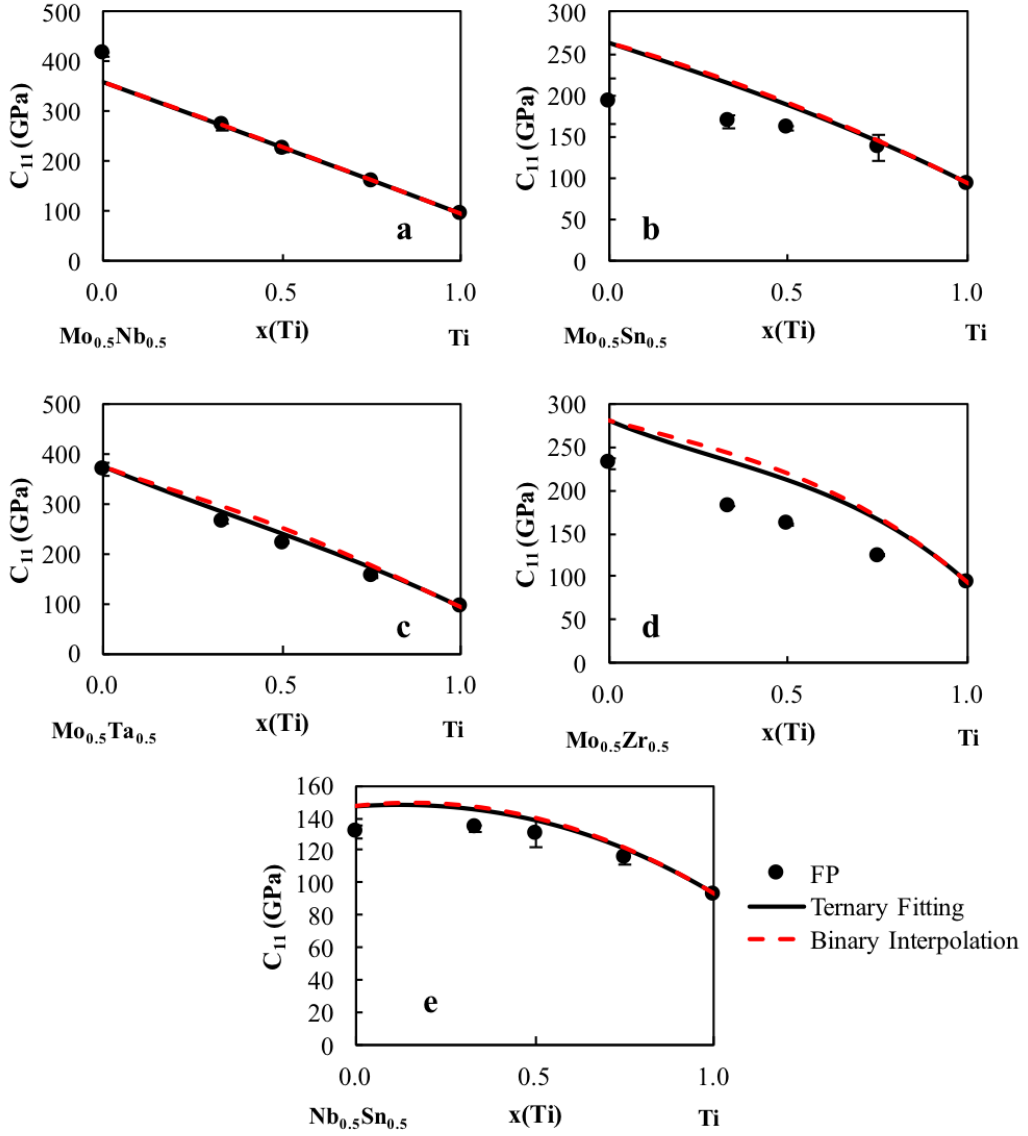


Figure 6.1: Calculated \bar{C}_{11} values (circles) plotted with their errors as well as the interpolation from the binary interaction parameters (red dashed line) and the ternary fitting (black dashed line) for five of the Ti-X-Y binary systems from a 50-50 mixture of the alloying elements $X_{0.5}Y_{0.5}$ to Ti ($X \neq Y = \text{Mo, Nb, Ta, Sn, Zr}$).

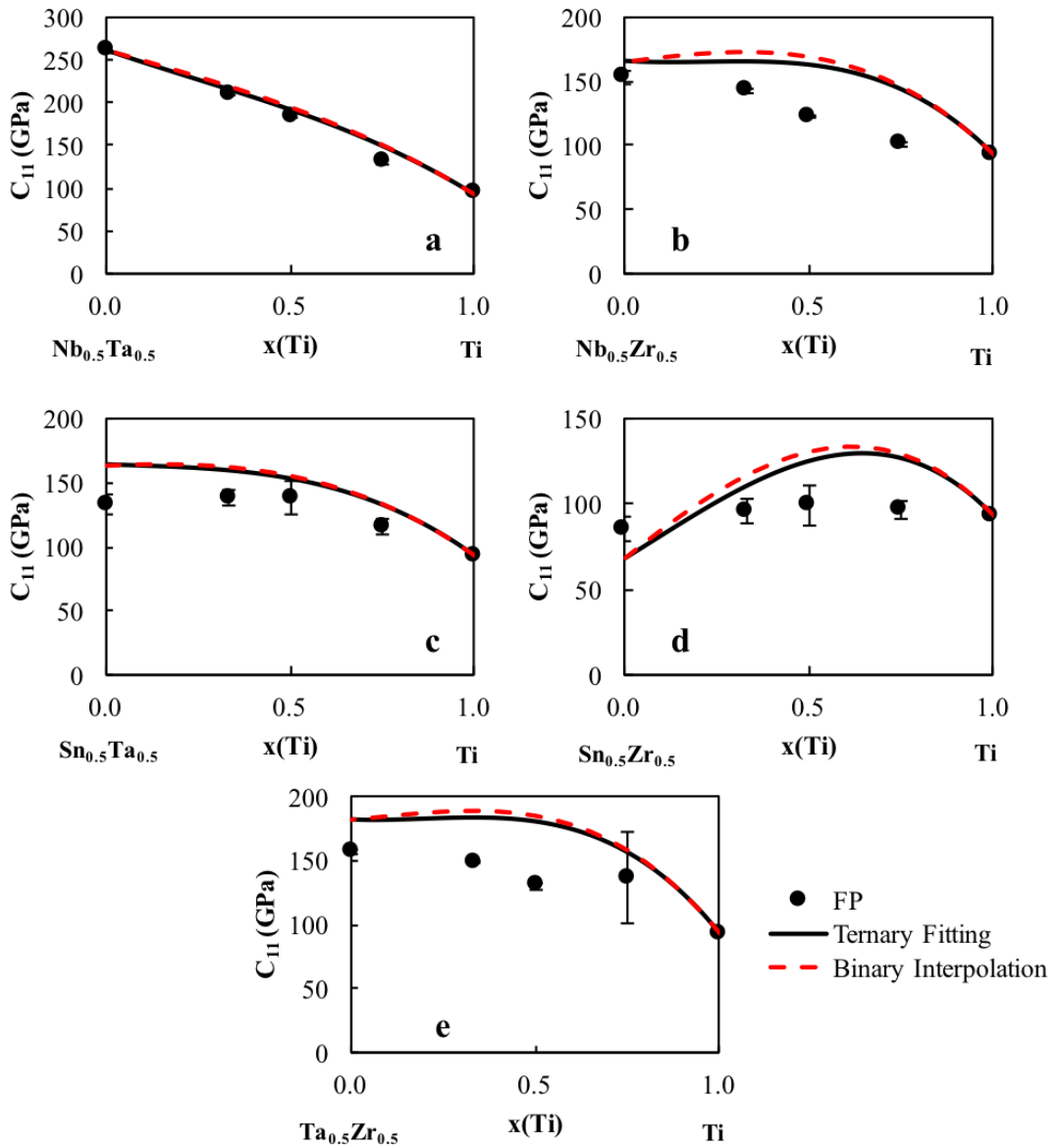


Figure 6.2: Calculated \bar{C}_{11} values (circles) plotted with their errors as well as the interpolation from the binary interaction parameters (red dashed line) and the ternary fitting (black dashed line) for five of the Ti-X-Y binary systems from a 50-50 mixture of the alloying elements $X_{0.5}Y_{0.5}$ to Ti ($X \neq Y = \text{Mo, Nb, Ta, Sn, Zr}$).

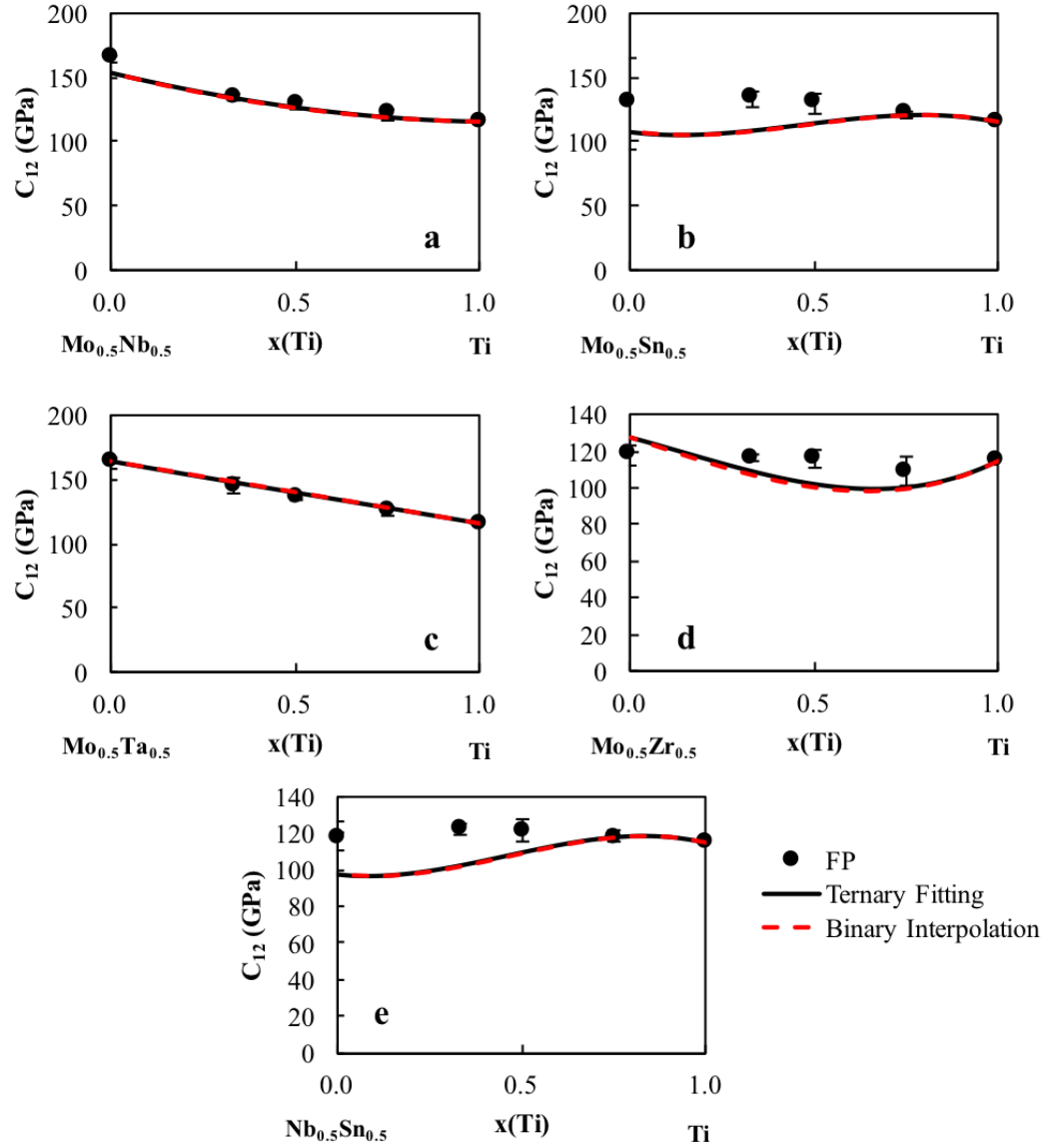


Figure 6.3: Calculated \overline{C}_{12} values (circles) plotted with their errors as well as the interpolation from the binary interaction parameters (red dashed line) and the ternary fitting (black dashed line) for five of the Ti-X-Y binary systems from a 50-50 mixture of the alloying elements X_{0.5}Y_{0.5} to Ti ($X \neq Y = \text{Mo, Nb, Ta, Sn, Zr}$).

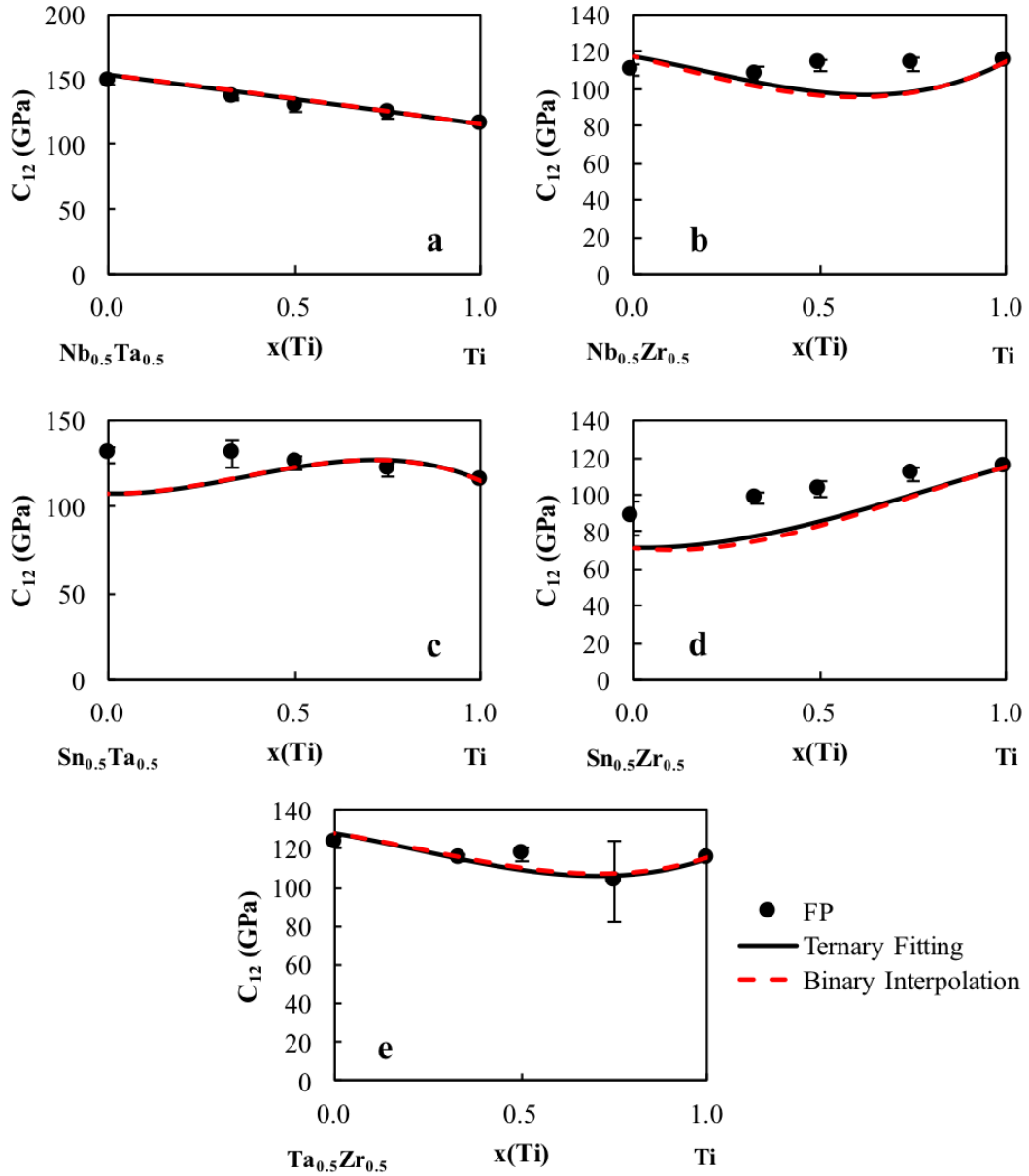


Figure 6.4: Calculated \bar{C}_{12} values (circles) plotted with their errors as well as the interpolation from the binary interaction parameters (red dashed line) and the ternary fitting (black dashed line) for five of the Ti-X-Y binary systems from a 50-50 mixture of the alloying elements $X_{0.5}Y_{0.5}$ to Ti ($X \neq Y = \text{Mo, Nb, Ta, Sn, Zr}$).

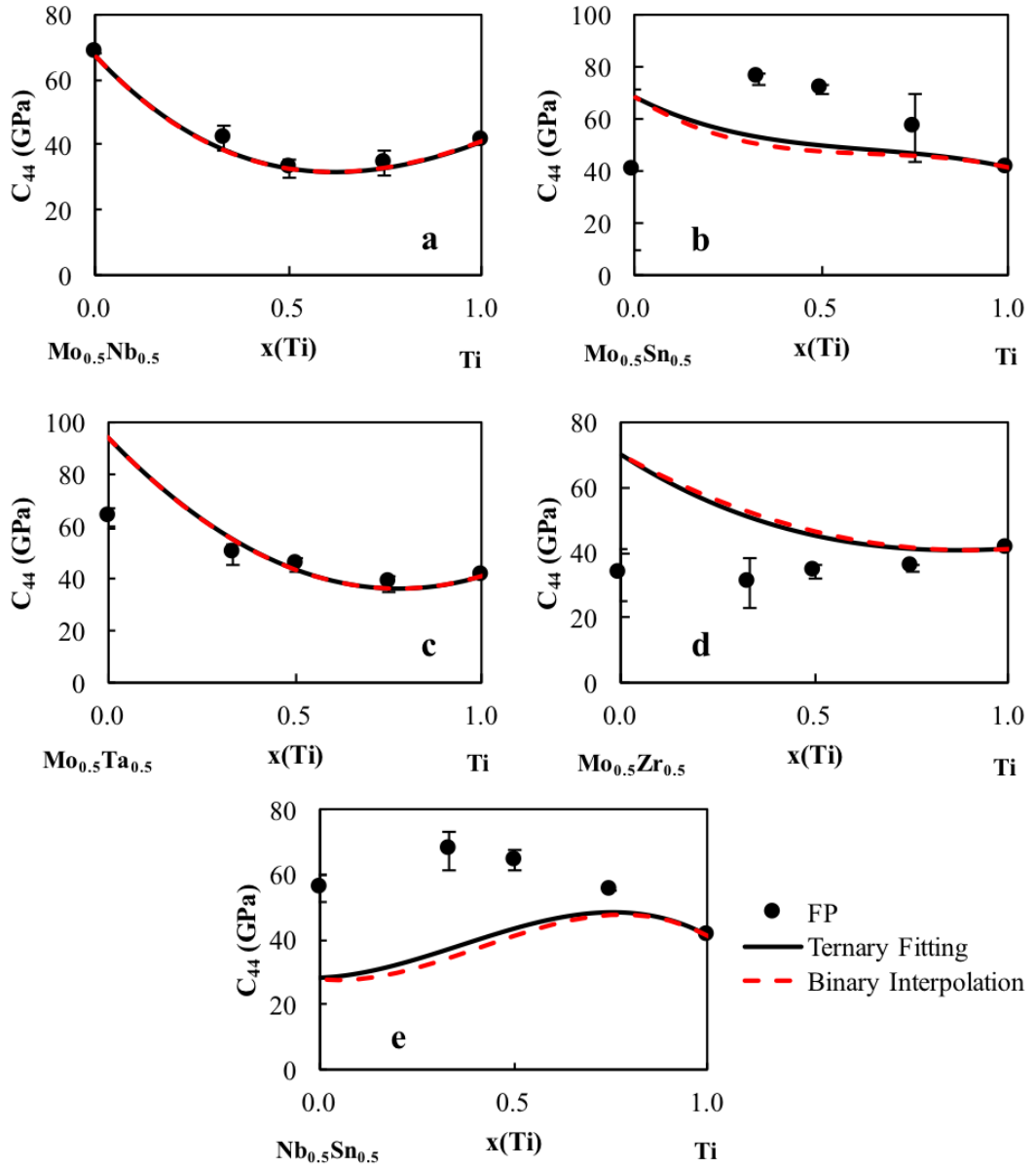


Figure 6.5: Calculated \overline{C}_{44} values (circles) plotted with their errors as well as the interpolation from the binary interaction parameters (red dashed line) and the ternary fitting (black dashed line) for five of the Ti-X-Y binary systems from a 50-50 mixture of the alloying elements $X_{0.5}Y_{0.5}$ to Ti ($X \neq Y = \text{Mo}, \text{Nb}, \text{Ta}, \text{Sn}, \text{Zr}$).

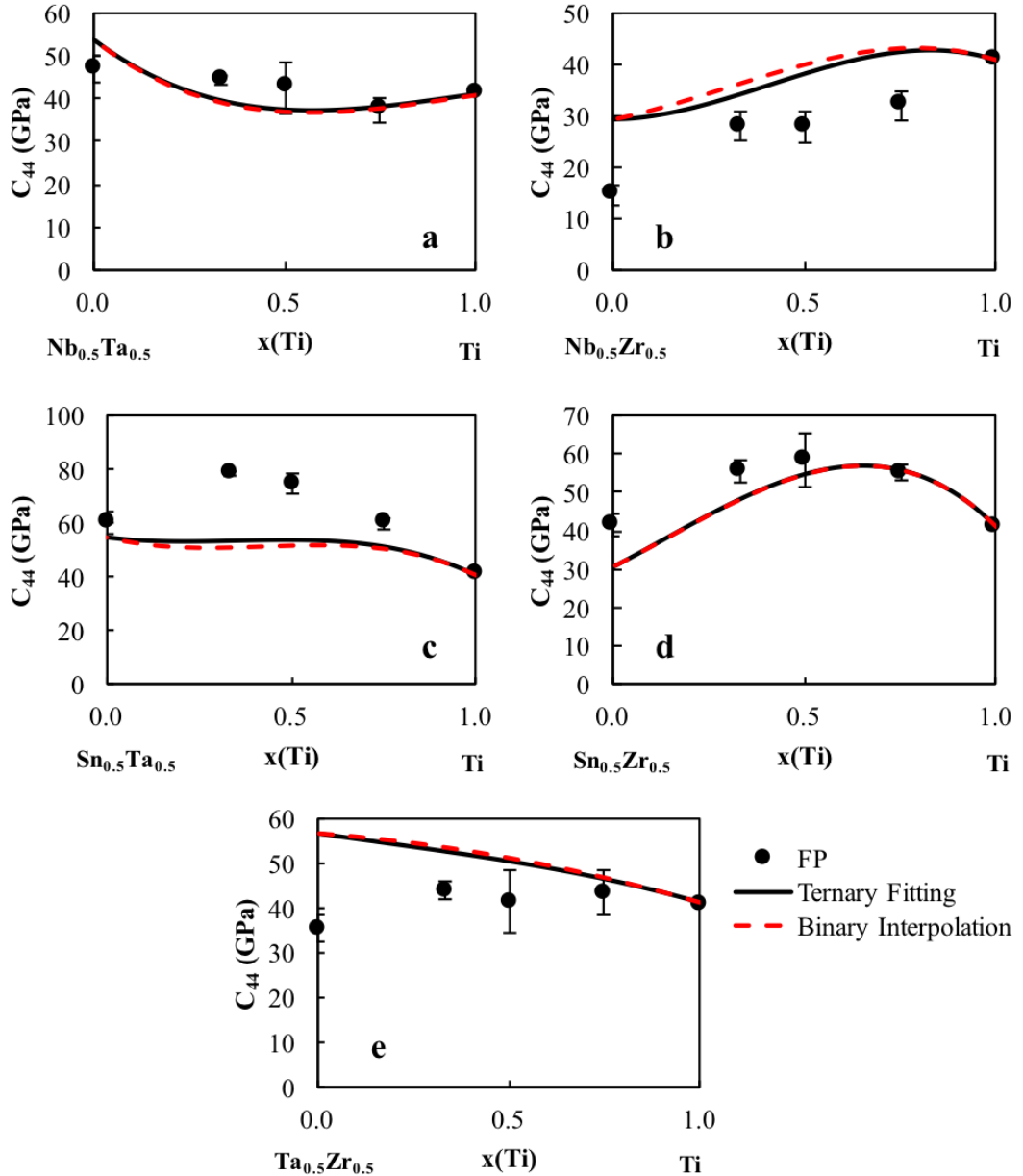


Figure 6.6: Calculated \bar{C}_{44} values (circles) plotted with their errors as well as the interpolation from the binary interaction parameters (red dashed line) and the ternary fitting (black dashed line) for five of the Ti-X-Y binary systems from a 50-50 mixture of the alloying elements $X_{0.5}Y_{0.5}$ to Ti ($X \neq Y = \text{Mo, Nb, Ta, Sn, Zr}$).

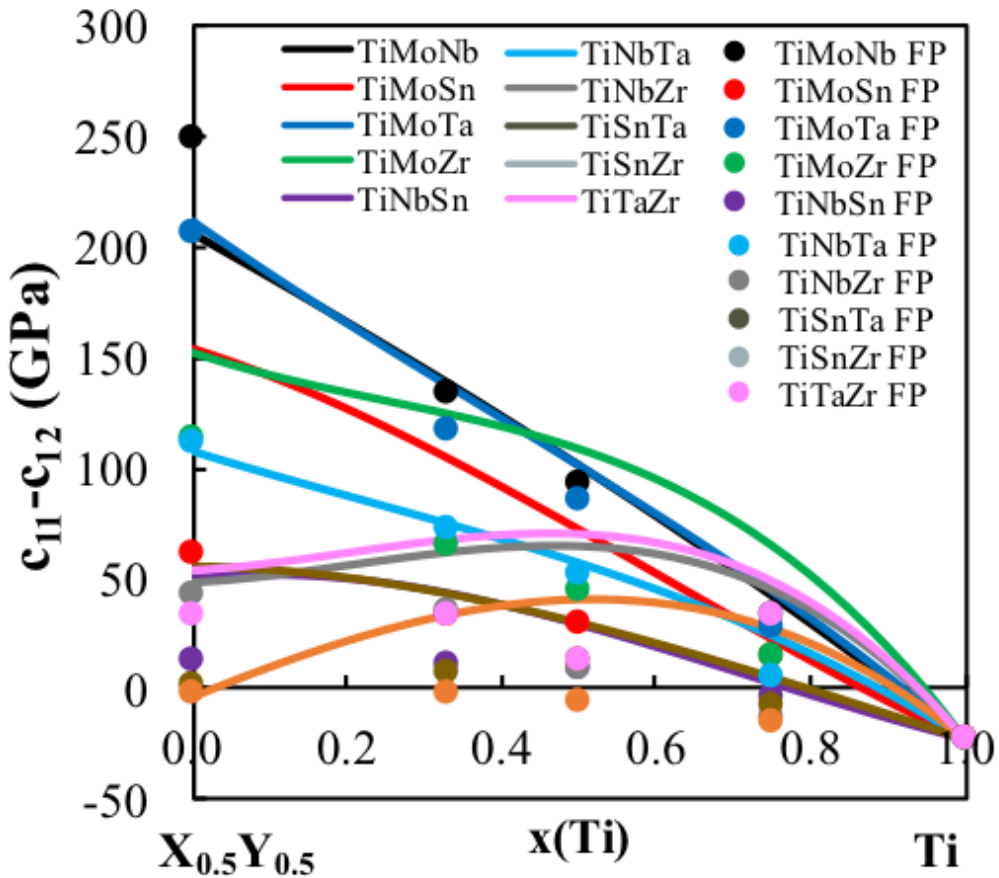


Figure 6.7: Calculated \bar{C}_{11} - \bar{C}_{12} values (circles) plotted with the present modeling (solid lines) for the Ti-X-Y ternary systems ($X \neq Y = Mo, Nb, Ta, Sn, Zr$). The \bar{C}_{11} - \bar{C}_{12} shows the stability of the bcc phase, when the value is negative the bcc phase is not stable in the corresponding composition ranges.

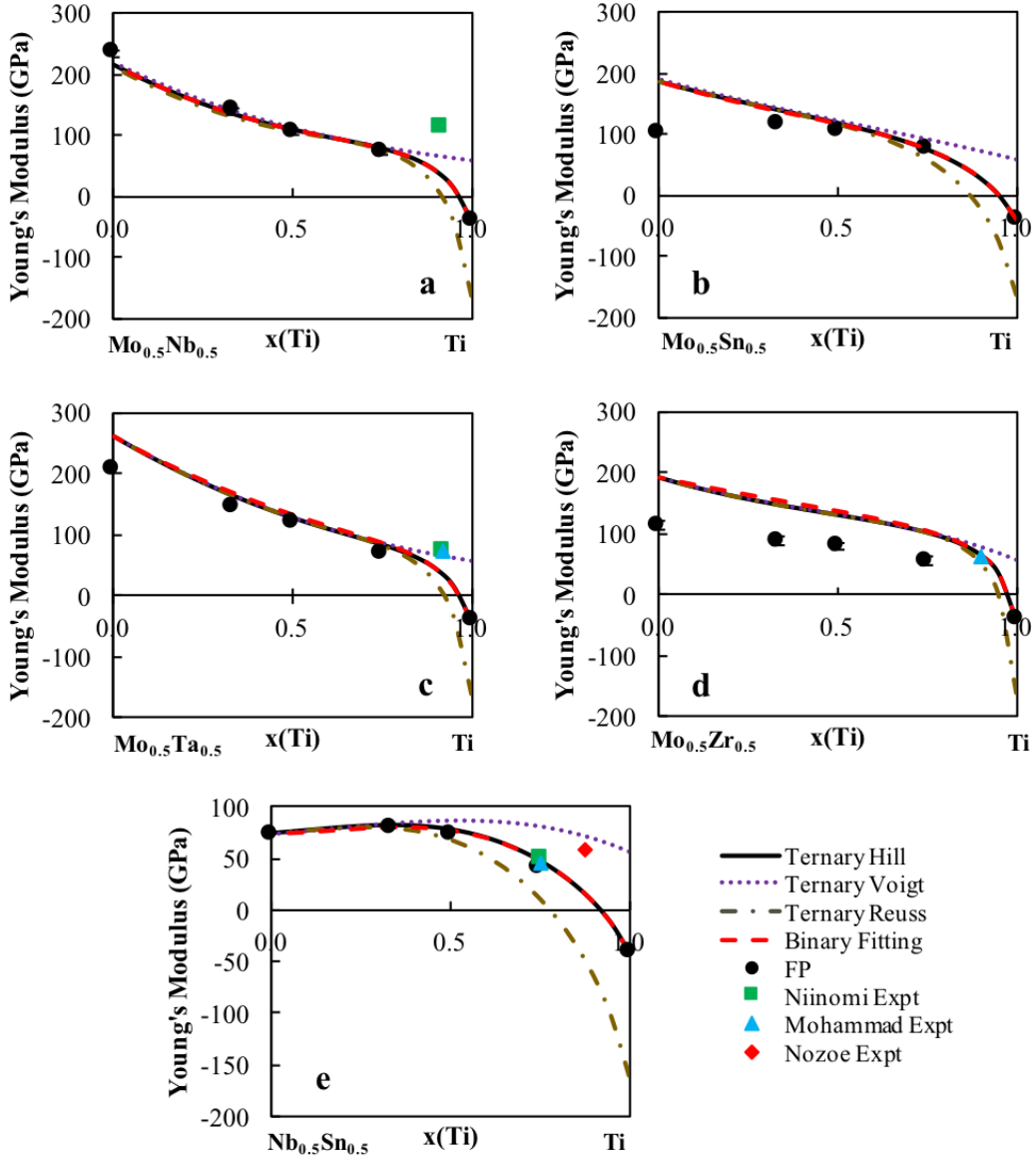


Figure 6.8: E of five of the Ti-X-Y ternary systems are plotted from a 50-50 mixture of the alloying elements to Ti in the bcc phase. The present calculations are plotted as filled circles with the error bars. The red dotted line is the extrapolation for the pure elements and binary interaction parameters only. The dotted purple line is the Voigt upper E bound, the gold dot dashed line is the lower Reuss E bound and the black line is the Hill E average. Experimental values are included for comparison [38–41].

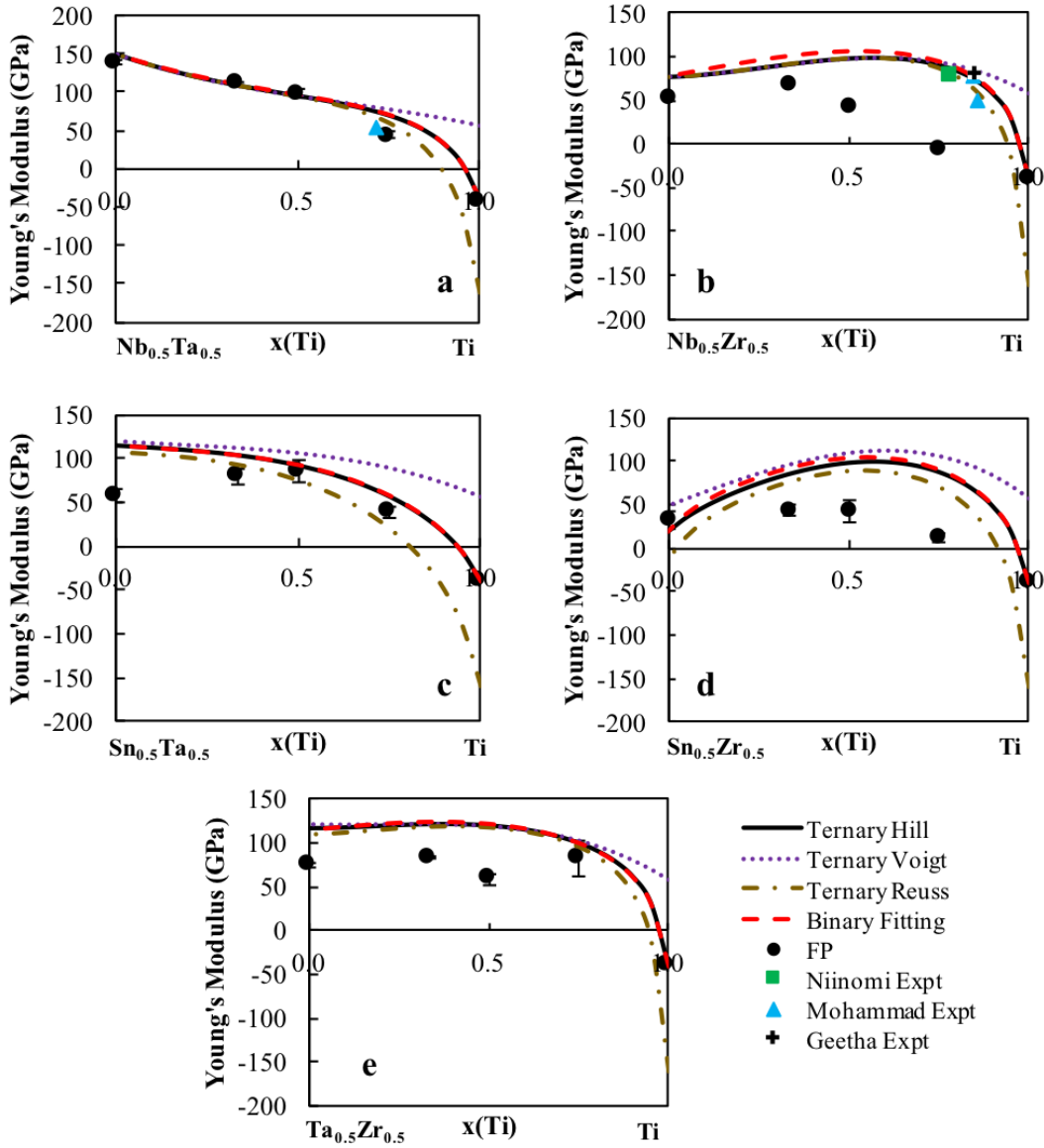


Figure 6.9: E of five of the Ti-X-Y ternary systems are plotted from a 50-50 mixture of the alloying elements to Ti in the bcc phase. The present calculations are plotted as filled circles with the error bars. The red dotted line is the extrapolation for the pure elements and binary interaction parameters only. The dotted purple line is the Voigt upper E bound, the gold dot dashed line is the lower Reuss E bound and the black line is the Hill E average. Experimental values are included for comparison [38–41].

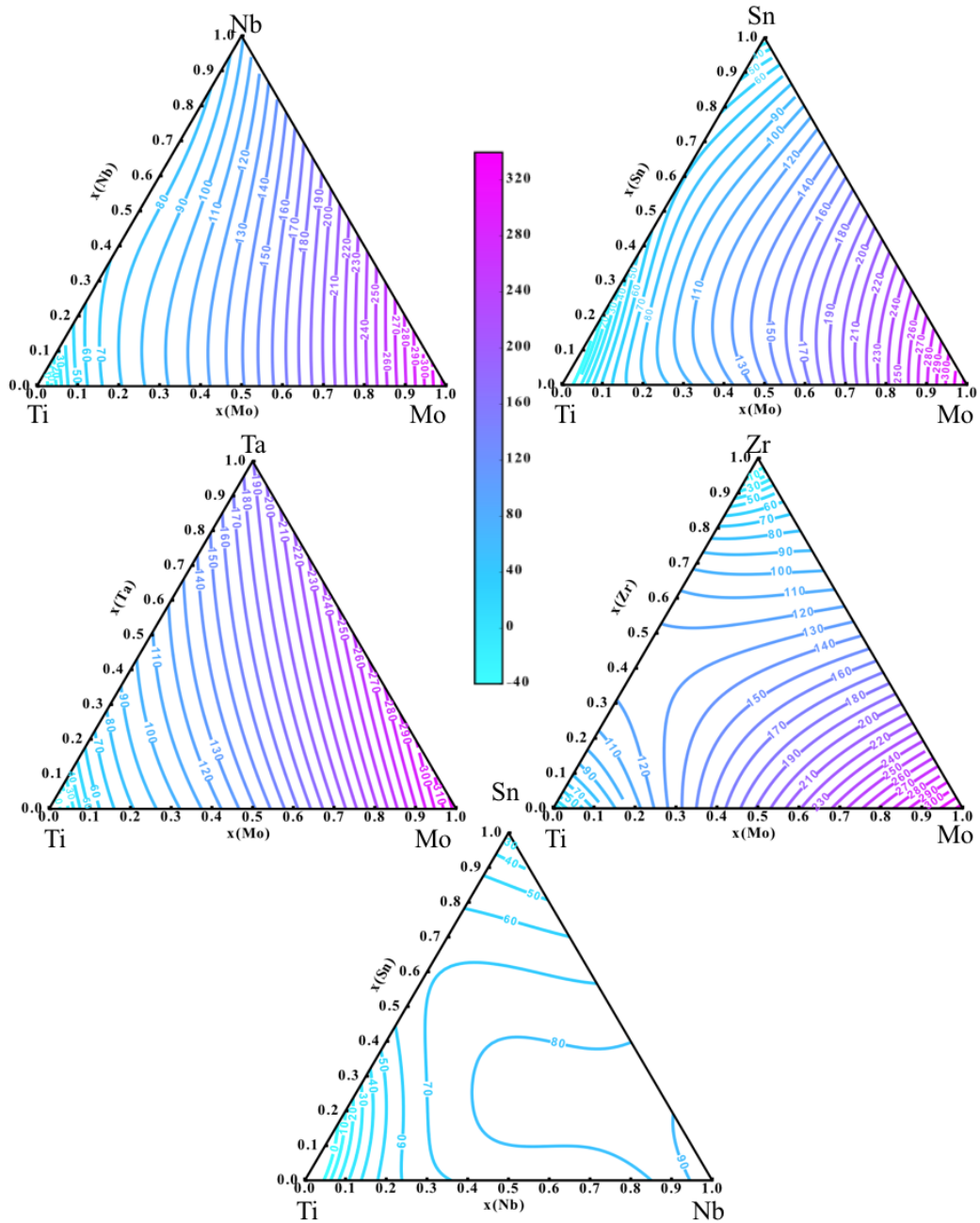


Figure 6.10: The Young's modulus is mapped as a function of composition in GPa for the Ti-Mo-Nb, Ti-Mo-Sn, Ti-Mo-Ta, Ti-Mo-Zr and Ti-Nb-Sn alloy systems using pycalphad [42].

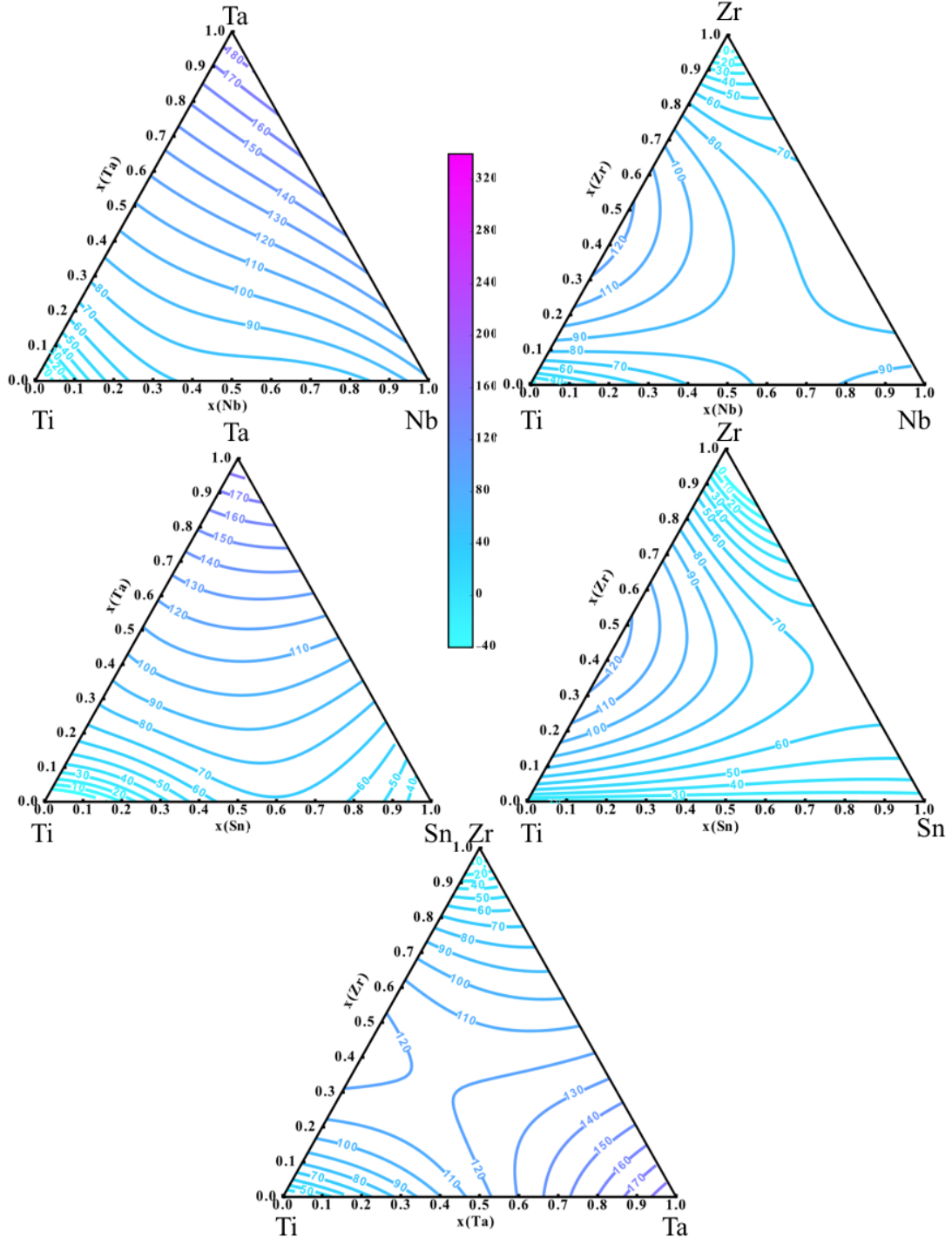


Figure 6.11: The Young's modulus is mapped as a function of composition in GPa for the Ti-Mo-Nb, Ti-Mo-Sn, Ti-Mo-Ta, Ti-Mo-Zr and Ti-Nb-Sn alloy systems using pycalphad [42].

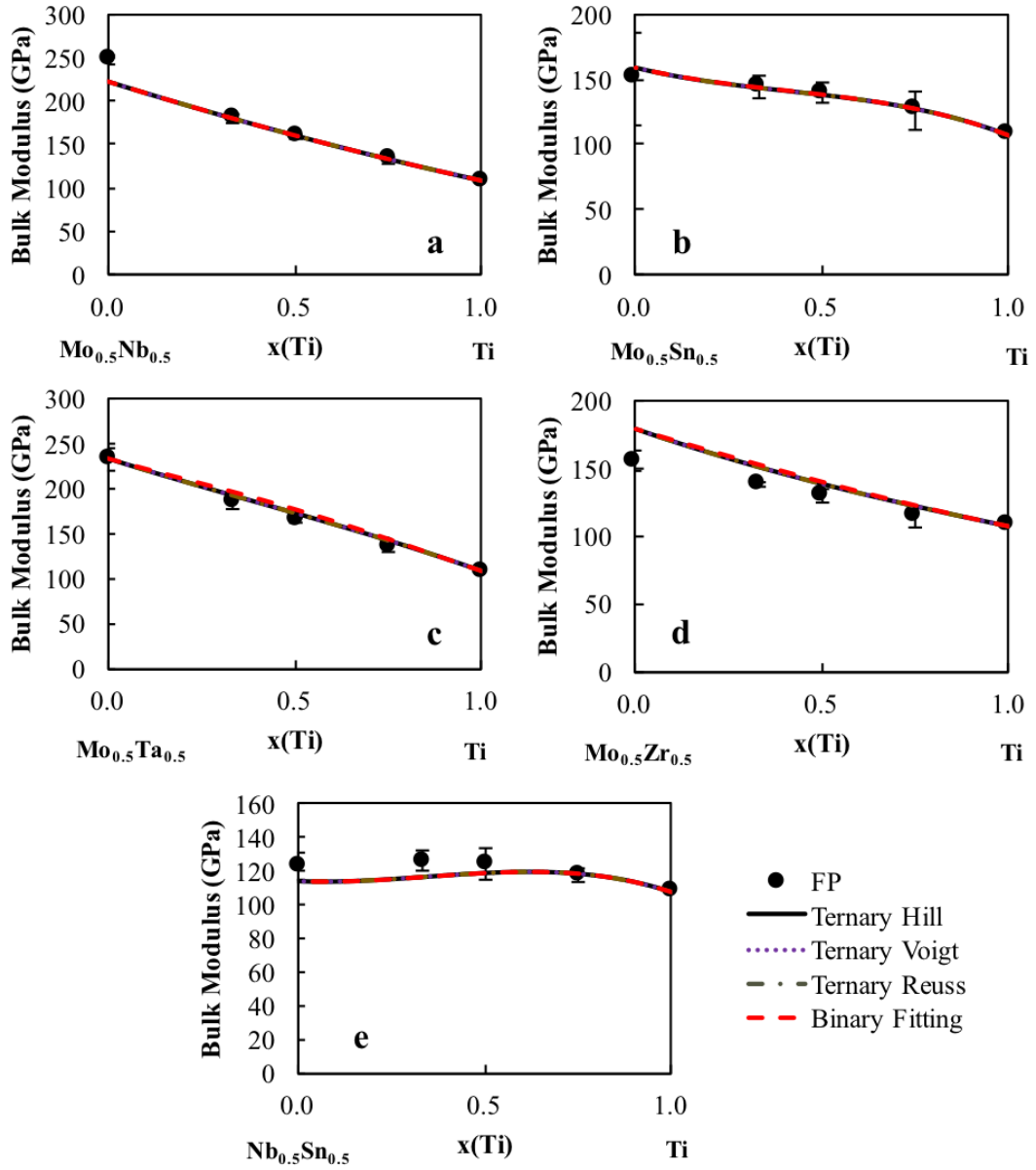


Figure 6.12: B are plotted from a 50-50 mixture of alloying elements $X_{0.5}Y_{0.5}$ to Ti in the bcc phase of five of the Ti-X-Y ternary systems ($X \neq Y = \text{Mo, Nb, Ta, Sn, Zr}$). The present calculations are plotted as the filled circles with error bars as well as the interpolation from the binary interaction parameters (red dashed line). The dotted purple line is the Voigt upper B bound, the gold dashed line is the lower Reuss B bound and the black line is the Hill B average.

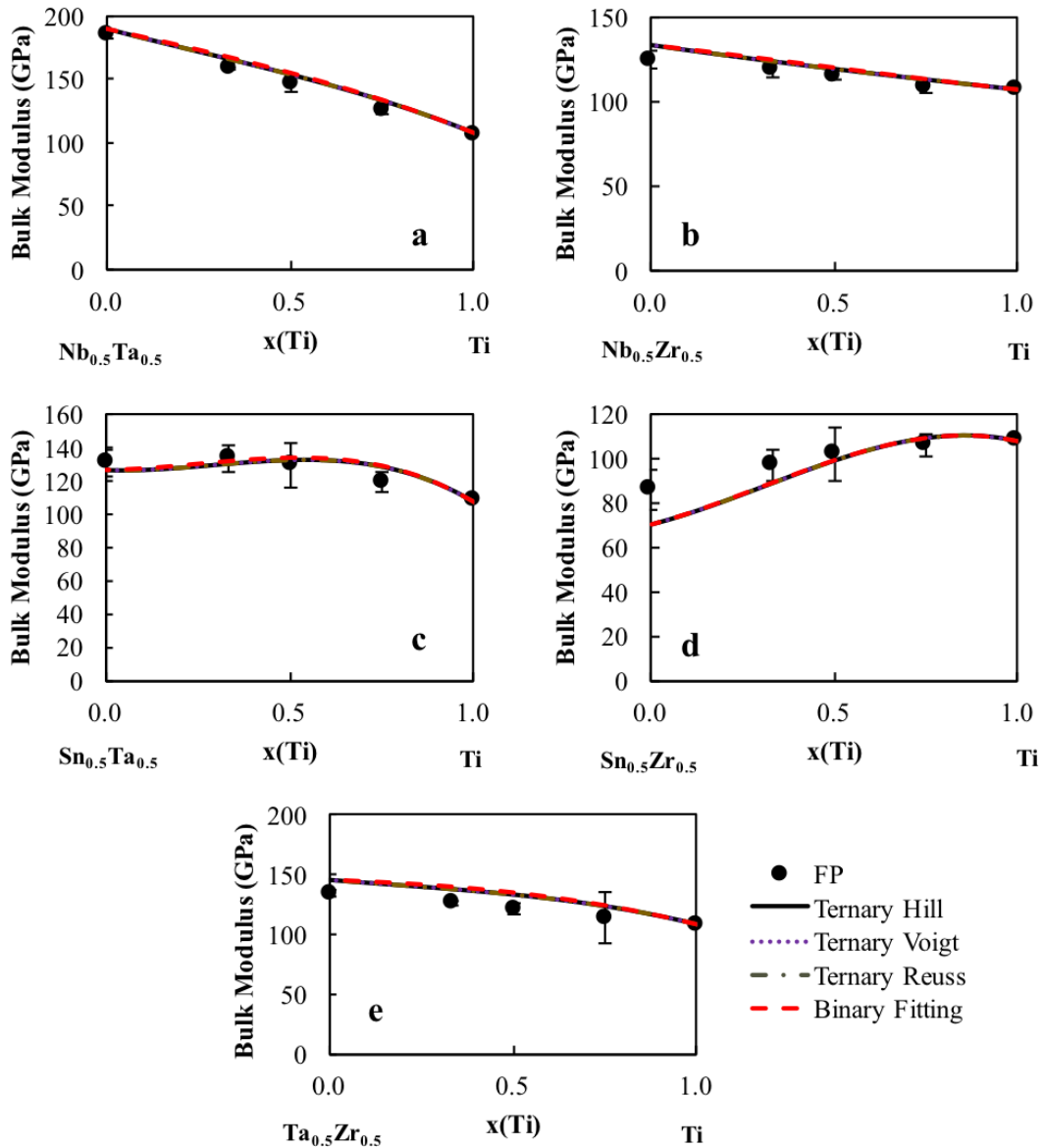


Figure 6.13: B are plotted from a 50-50 mixture of alloying elements $X_{0.5}Y_{0.5}$ to Ti in the bcc phase of five of the Ti-X-Y ternary systems ($X \neq Y = \text{Mo, Nb, Ta, Sn, Zr}$). The present calculations are plotted as the filled circles with error bars as well as the interpolation from the binary interaction parameters (red dashed line). The dotted purple line is the Voigt upper B bound, the gold dashed line is the lower Reuss B bound and the black line is the Hill B average.

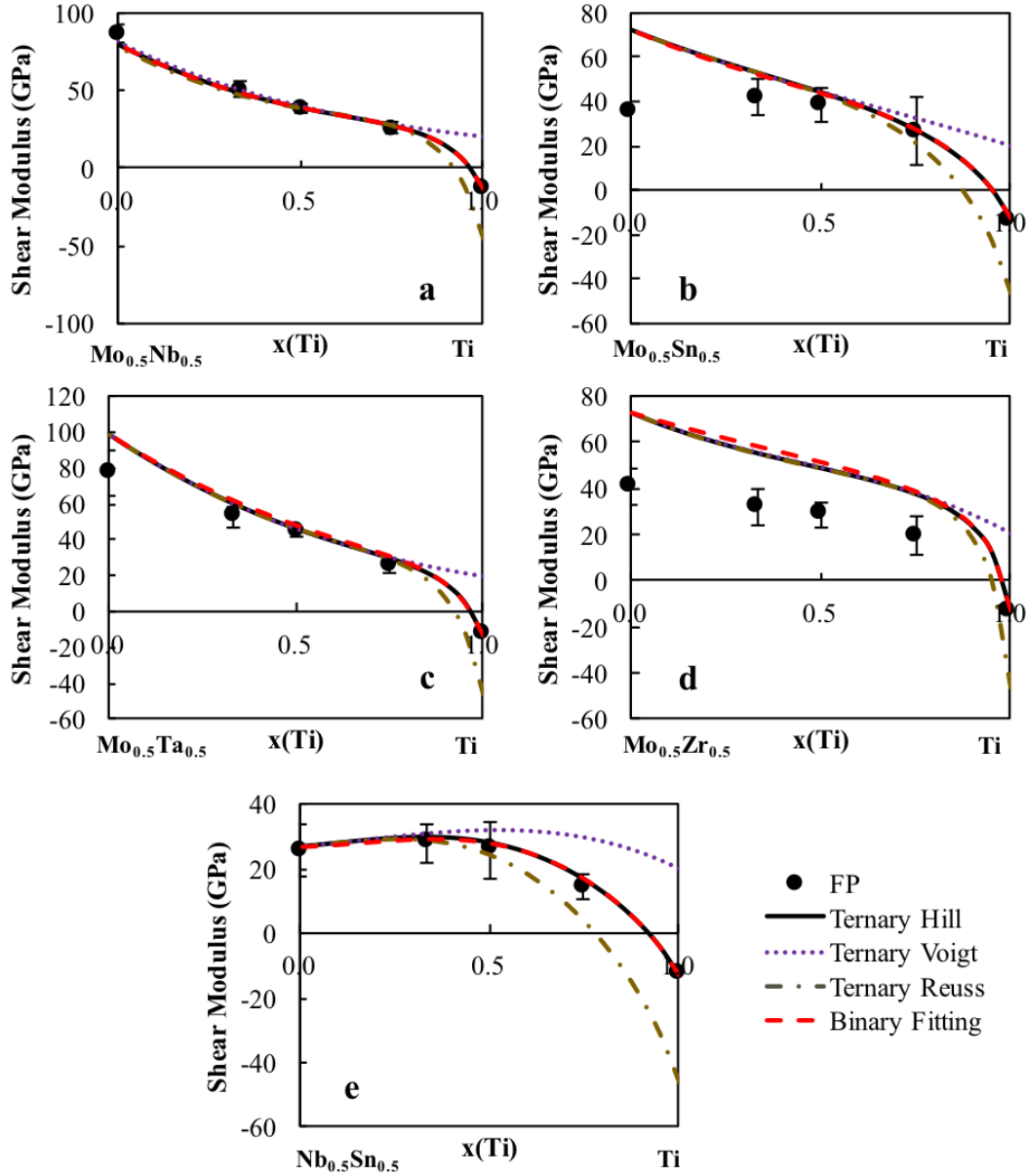


Figure 6.14: G are plotted from a 50-50 mixture of alloying elements $X_{0.5}Y_{0.5}$ to Ti in the bcc phase of five of the Ti-X-Y ternary systems ($X \neq Y = \text{Mo, Nb, Ta, Sn, Zr}$). The present calculations are plotted as the filled circles with error bars as well as the interpolation from the binary interaction parameters (red dashed line). The dotted purple line is the Voigt upper G bound, the gold dashed line is the lower Reuss G bound and the black line is the Hill G average.

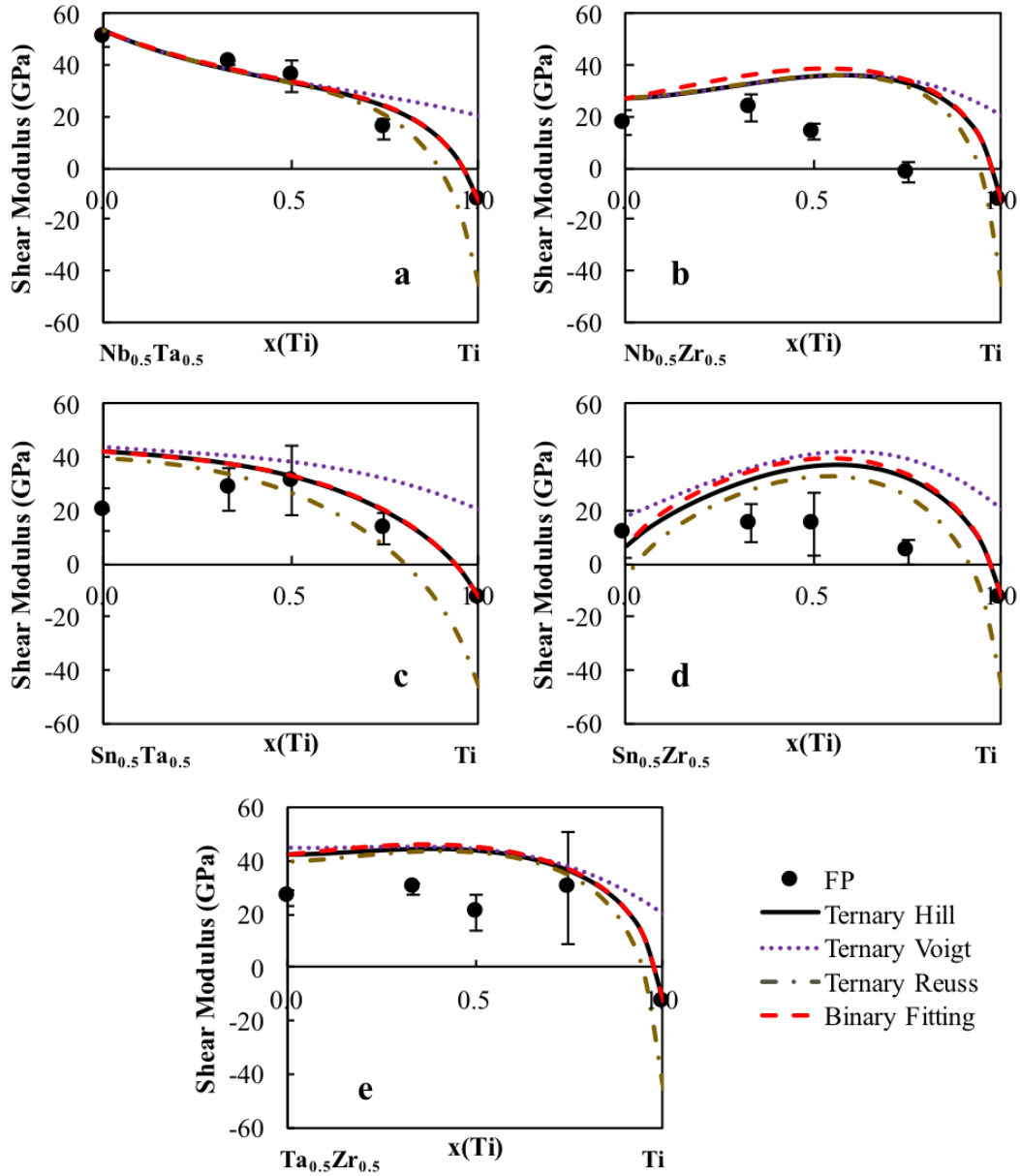


Figure 6.15: G are plotted from a 50-50 mixture of alloying elements $X_{0.5}Y_{0.5}$ to Ti in the bcc phase of five of the Ti-X-Y ternary systems ($X \neq Y = \text{Mo, Nb, Ta, Sn, Zr}$). The present calculations are plotted as the filled circles with error bars as well as the interpolation from the binary interaction parameters (red dashed line). The dotted purple line is the Voigt upper G bound, the gold dashed line is the lower Reuss G bound and the black line is the Hill G average.

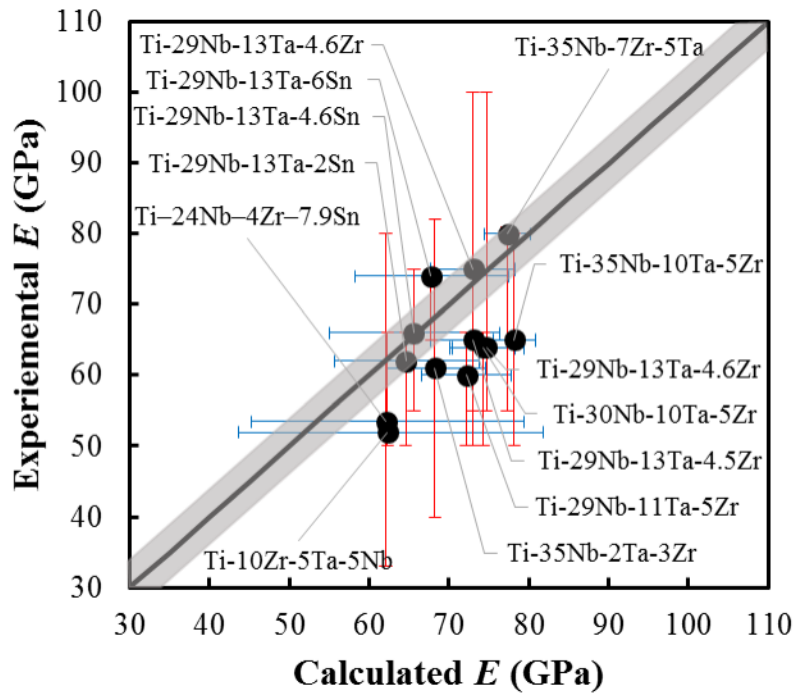


Figure 6.16: E of multicomponent bcc Ti alloys predicted from the database are compared with measured experimental results. Error bars plotted are from the variation in experimentally determined Young's moduli values for the specific multi-component alloy. The grey region refers to the error in the first-principles calculations. More information on the alloys is Table 6.4 [37–39].

Chapter 8 |

Conclusions and Future Work

8.1 Conclusions

In this dissertation, the effect of alloying elements on Ti-based alloys was systematically studied. The work began by using first-principles based DFT calculations and the CALPHAD method to study the effect that the alloying elements Mo, Nb, Sn, Ta and Zr have on the equilibrium phase stability, thermodynamics, and elastic properties. The work uses the equation of states fitting of the energy vs. volume curves to get the ground state equilibrium properties. The Debye-Grüneisen model and phonon quasiharmonic approach were used to study the effect of temperature on the phase stability. A new theoretic framework was proposed to study the formation of the metastable phases. The accuracy of the theoretic framework and the transformation that occurs when these metastable phases form was studied using neutron scattering experiments. The compilation of the work develops a knowledge base for Ti-based alloys and will help to guide the future design of biocompatible implants. The main conclusions from this work are included below:

1. A compatible thermodynamic database for the Ti-Mo-Nb-Sn-Ta-Zr system was built using descriptions of five pure elements (Ti, Mo, Nb, Ta, Zr), ten binary systems (Ti-Mo, Ti-Nb, Ti-Ta, Ti-Zr, Mo-Nb, Mo-Ta, Mo-Zr, Nb-Ta, Nb-Zr, Ta-Zr), and six Ti-containing ternary systems (Ti-Mo-Nb, Ti-Mo-Ta, Ti-Mo-Zr, Ti-Nb-Ta, Ti-Nb-Zr, Ti-Ta-Zr). Sn was excluded from the database due to the lack of modeling for the Sn binary systems. The Ta-Sn and Mo-Sn system lacked a thermodynamic description and the thermodynamic modeling of the Sn-Zr system is incompatible with the current database. The present

work began modeling the Sn binaries with the Ta-Sn system discussed chapter 4. Until the binaries are properly modeled Sn was not included in the database which shouldn't affect the use of the database for biomedical applications since Sn will only be added to biomedical alloys in small percentages. The thermodynamic descriptions of the pure elements were adopted from the SGTE database [32]. All of the binary systems had previous thermodynamic descriptions available and the compatible descriptions were evaluated for accuracy and incorporated into the database. The binary interpolations of the Ti-containing ternary systems were plotted and compared with the available experimental data as well as the enthalpy of formation of the bcc phase calculated from first-principles based on DFT. The Ti-Sn-X systems ($X = \text{Mo, Nb, Ta, Zr}$) will be modeled in the future work once the Sn binaries are modeled. The binary interpolations of the Ti-Nb-Zr and Ti-Ta-Zr systems had previously been plotted but no interaction parameters had been introduced. The present evaluation agreed with the previous evaluations and no ternary interaction parameters were introduced. The Ti-Mo-Zr system had previously been modeled and the present work agreed with the evaluation. The Ti-Mo-Nb, Ti-Mo-Ta and Ti-Nb-Ta systems had never previously been modeled. The present work evaluated interaction parameters for the Ti-Mo-Ta and Ti-Nb-Ta systems but didn't introduce any interaction parameters for the Ti-Mo-Nb system. The thermodynamic descriptions were all incorporated into a complete database that accurately predicts the phase stability of the Ti-Mo-Nb-Sn-Ta-Zr systems. The completed database is in appendix A.

2. Sn-Ta modeling was completed using data from DFT-based first-principles calculations and the available experimental data in the literature to model the Gibbs energies for the bcc and liquid solution phases and the stoichiometric Ta_3Sn and TaSn_2 phases of the Sn-Ta system. First-principles calculations were used to predict the enthalpy of formation of the bcc phase for the evaluation of interaction parameters in the phase. The decomposition temperature of Ta_3Sn was predicted to be 2884 °K. The completed thermodynamic description was complied into a tdb file in appendix B.
3. The effects of five alloying elements on the elastic properties of bcc Ti-X ($X = \text{Mo, Nb, Sn, Ta, Zr}$) alloys, including the elastic stiffness constants, bulk

modulus, shear modulus, and Young's modulus, were systematically studied using first-principles calculations. The CALPHAD methodology was used to evaluate interaction parameters to predict the elastic properties as a function of composition. The calculations showed that 5.5, 11.5, 51.5, 9.5, and 4.0 at. % of Mo, Nb, Sn, Ta and Zr, respectively, were required to stabilize the bcc phase according to the Born criteria. The trends observed were summarized for each Ti-X (X= Mo, Nb, Sn, Ta, Zr) binary system. Alloying with Mo, Nb, and Ta results in similar trends, which is probably because Mo, Nb, and Ta are strong bcc stabilizers and stable in the bcc structure at room temperature. The interaction parameters determined in the current work were used to predict the elastic properties of higher order alloys. The accuracy of database predictions of the Young's modulus was evaluated by comparing the calculated and experimental Young's moduli. Overall, the database provides good predictions of the elastic properties of Ti-alloys in the bcc phase as a function of composition.

4. The elastic properties of the bcc Ti-X-Y ternary alloys ($X \neq Y = \text{Mo, Nb, Sn, Ta, Zr}$), including the elastic stiffness constants, bulk modulus, shear modulus, and Young's modulus were systematically studied using first-principles based on DFT calculations. The general CALPHAD modeling approach was used to fit ternary interaction parameters. From the elastic stiffness constant data, the Ti-X-Y ($X \neq Y = \text{Mo, Nb, Ta}$) show the same trends in the data. This is to be expected because Mo, Nb, and Ta are similar elements that are strong β -stabilizers and stable in the bcc phase at low temperatures. It was also seen that the Ti-X-Sn ($X = \text{Mo, Nb, Ta}$) alloys showed similar trends in the data for most of the elastic stiffness constants, so do the Ti-X-Zr ($X = \text{Mo, Nb, Ta}$) alloys. The present calculations showed that the bcc Ti-alloy was mechanically stabilized at compositions less than 91, 92, 95, 93, 91, 94, 87, 77, 89, and 80 at % Ti for the Ti-Mo-Nb, Ti-Mo-Ta, Ti-Mo-Zr, Ti-Nb-Zr, Ti-Sn-Zr, Ti-Ta-Zr, Ti-Mo-Sn, Ti-Nb-Sn, Ti-Nb-Ta and Ti-Sn-Ta alloys, respectively. As discussed above, Mo, Nb and Ta are strong β -stabilizers and thus the Ti-Mo-Nb, Ti-Mo-Ta, and Ti-Nb-Ta systems stabilize the bcc phase similarly. Also, discussed previously, Zr is a weak β -stabilizer alone but when alloyed with other elements it acts a strong β -stabilizer. This is observed with the Ti-Mo-Zr, Ti-Nb-Zr, Ti-Ta-Zr systems all stabilizing the bcc phase at

high Ti concentrations (95, 93, and 94 at.% respectively). Zr was even able to stabilize the Ti-Sn-Zr system at a high Ti concentration of 91 at.% Ti, even with Sn not being a *beta*-stabilizer or stable in the bcc phase. The ternary interaction parameters were combined with the previously determined pure elements and binary interaction parameters to map some of the possible alloy compositions to find potential materials with a Young's modulus in the target range for biomedical load-bearing implants. Overall, the introduction of the ternary interaction parameters improved the database's ability to predict the E of higher order alloys by a small amount. The complete database is in appendix D and satisfactorily predicts the elastic properties of higher order Ti-alloys.

5. The elastic stiffness constants and Young's moduli of the Ti-Nb system in the bcc, hcp, ω , and α'' phases was systematically calculated using first-principles based on DFT. The general CALPHAD modeling approach was used to fit binary interaction parameters. The E values were similar for the hcp and ω phase, which is reasonable since they both have hexagonal symmetry. The α'' phase has E values that were higher than the other three phases which explains why the E increases when the α'' phase forms. Experiments showed that up to 10 at. % Nb the samples formed solely the hcp phase and the database predicted the E values by an average variance of 8 GPa from the experimental E . The samples from 10 at. % Nb to 30 at. % Nb formed the bcc and α'' or ω phases. If the samples were slow cooled they form the bcc and ω phases. If the samples were quenched they form the bcc and α'' phases. Using experimentally determined phase fractions and the rule of mixtures, the database accurately predicted the E values by an average variance of 0.52 GPa when compared with the experimental E values. At Nb concentrations greater than 30 at. % Nb samples form solely the bcc phase and the database predicted the E values by an average variance of 7 GPa from the experimental E values. The phonon DOS of the slow cooled samples and the phonon DOS of the quenched samples were plotted together for the same compositions and showed differences that were expected for the samples have different phases. This difference was also seen when looking at the entropy difference between the two samples. The entropy difference between the quenched and slow cooled samples increased from 10 at. % Nb to 20 at. % Nb. This increase in

entropy difference must be investigated further in order to understand this observation. Using the diffraction patterns, the phase fractions of each sample were approximated. The implementation of the partition function approach is in progress but the results presented here show that the elastic database can accurately asses the Young's moduli and elastic stiffness constants of Ti-Nb alloys if the phase fractions of the metastable phases can be predicted.

8.2 Future Work

The following are presented as future work to be able to improve this thesis work:

1. Focusing on the modeling of the Sn binary and Ti-Sn-X (X = Mo, Nb, Ta, Zr) and incorporating them into this database would further improve the knowledge base of Ti-alloys that this thesis presents. As discussed, Sn is being added due to its low cost and the fact that at low concentrations it doesn't effect the alloys biocompatibility. But even at low compositions having a better understanding of how Sn effects the phase stability would be helpful.
2. As discussed, introducing interaction parameters to describe the elastic properties for the non Ti-containing binary and ternary systems and the hcp would improve the databases accuracy and extend its uses to other applications
3. The work on using the partition function approach will be continued. The next steps will be to calculate the helmholtz energies of all of the pure elements and to extend this to calculate better helmholtz energies for the metastable and unstable phases. The ability of the partition function approach to calculate more accurate entropies would be a great advancement in the field.
4. Study the temperature dependence of the phonon DOS to gain insight into the type of transformation occurring when α'' and ω form